FLOATECH

D1.1. Hybrid Eulerian-Lagrangian Aerodynamic Model

DATE OF DELIVERY - 28/02/2021

AUTHOR(S) – JOSEPH SAVERIN

TECHNICAL UNIVERSITY OF BERLIN

FLOATECH
THE FUTURE OF FLOATING WIND TURBINES

Document track details

Project acronym	FLOATECH
Project title	Optimization of floating wind turbines using innovative control techniques and fully coupled open-source engineering tool
Starting date	01.01.2021
Duration	36 months
Programme	H2020-EU.3.3.2. - Low-cost, low-carbon energy supply
Call identifier	H2020-LC-SC3-2020-RES-RIA
Grant Agreement No	101007142

Deliverable Information	
Deliverable number	D1.1
Work package number	WP1
Deliverable title	Hybrid Eulerian-Lagrangian Aerodynamic Model
Lead beneficiary	TU Berlin
Author	Joseph Saverin
Due date	28.02.2022
Actual submission date	28.02.2022
Type of deliverable	Report
Dissemination level	Public

Version management

Document history and validation			
Version	Name	Date	Comment
V 0.1	Saverin, J., TU Berlin	11/02/2022	First draft
V 0.2	Saverin, J., TU Berlin	22/02/2022	Updated draft internally reviewed
V1.0	Saverin, J., TU Berlin	26/02/2022	Final version

Background: about the FLOATECH project

The FLOATECH project is a Research and Innovation Action funded by the European Union's H2020 programme aiming to increase the technical maturity and the cost competitiveness of floating offshore wind (FOW) energy. This is particularly important because, due to the limitations of available installation sites onshore, offshore wind is becoming crucial to ensure the further growth of the wind energy sector.

The project is implemented by a European consortium of 5 public research institutions with relevant skills in the field of offshore floating wind energy and 3 industrial partners, two of which have been involved in the most recent developments of floating wind systems.

The approach of FLOATECH can be broken down into three actions:

- The development, implementation and validation of a user-friendly and efficient design engineering tool (named QBlade-Ocean) performing simulations of floating offshore wind turbines with an unseen combination of aerodynamic and hydrodynamic fidelity. The advanced modelling theories will lead to a reduction of the uncertainties in the design process and an increase of turbine efficiency.

- The development of two innovative control techniques (i.e. Active Wave-based feed-forward Control and the Active Wake Mixing) for Floating Wind Turbines and floaters, combining wave prediction and anticipation of induced platform motions. This is expected to improve the performance of each machine and to minimise wake effects in floating wind farms, leading to a net increase in the annual energy production of the farm.

- The economic analysis of these concepts to demonstrate qualitatively and quantitatively the impact of the developed technologies on the Levelized Cost of Energy (LCOE) of FOW technology.

In addition to the technological and economic impacts, the project is expected to have several impacts at societal, environmental and political levels, such as: public acceptance due to reduced noise and visibility issues of FOWT; very low impact on biodiversity and wildlife habitat because no piles are needed be to installed into the seabed; design choices requiring less material and space; the promotion of the installation of FOW in transitional water depths (30-50 meters), as the costs for FOW at those locations will become more competitive compared to the fixed bottom foundations.

Table of contents

Table of Contents

List of acronyms and abbreviations

Acronym / Abbreviation	Meaning / Full text
AoA	Angle of Attack
BEM	Boundary Element Method
CFD	Computational Fluid Dynamics
CPU	Central Processing Unit
DOF	Degrees of Freedom
FD	Finite Difference
FMM	Fast Multipole Method
FOW	Floating Offshore Wind
FOWT	Floating Offshore Wind Turbine
FV	Finite Volume
GPU	Graphical Processing Unit
LCOE	Levelized Cost of Energy
HPC	High-performance computing
LLFVW	Lifting Line free vortex wake
MLMIC	Multilevel Multi-Integration Cluster
OP	Operational Point
PIV	Particle Image Velocimetry
RWT	Reference Wind Turbine
QB	QBlade Ocean
TSR	Tip-Speed Ratio
VP	Vortex Particle
VPML	Vortex Particle Multilevel
WP	Work Package

EXECUTIVE SUMMARY

This document is a deliverable of the FLOATECH project, funded under the European Union's Horizon 2020 research and innovation programme under grant agreement No 101007142.

The design of a wind turbine requires a detailed mechanical analysis of the entire turbine system. The turbine must be capable of safely operating within a broad load envelope, in a number of operating states while consistently generating an optimal electrical output. These loads vary greatly as a function of turbine size, environmental conditions and turbine architecture. The current interest in floating offshore architectures implies that the complexity of the simulated systems increases. The dynamics of the turbine are significantly more complex than the equivalent onshore or fixed bottom-offshore scenarios as the entire turbine assembly becomes mechanically coupled with the sea state and dynamics of the floater assembly and mooring lines. These couplings influence the dynamical response of the turbine. A holistic treatment of the problem is required in order to ensure the correct estimation of load envelopes and safety margins.

The inherent complexity of this dynamic system quickly limits the applicability of closed-form expressions and necessitates simulation with numerical methods. This has given rise in recent decades to a range of simulation tools and software packages aimed at addressing this issue. The state-of-the-art of current simulation packages must be advanced in order to allow for simulation of floating offshore architectures to ensure that turbine design iterations can be carried out efficiently. These advances must occur in a range of disciplines including hydrodynamic, structural and aerodynamic modelling. This report focusses on the latter, and introduces a new numerical method for simulating the aerodynamics of wind turbines.

The simulation of aerodynamic loads acting on a floating offshore device introduces unique challenges. The relative motion of the floating turbine system can give rise to a stronger interaction of the turbine rotor with its own wake. Furthermore, the influence of environmental conditions in offshore environments are markedly different to equivalent onshore scenarios as a result of the fundamentally different behaviour of the atmospheric boundary layer and surface roughness effects. The turbine wake can remain stable for a greater downstream distance in comparison with onshore scenarios [64], potentially increasing aerodynamic interaction between turbines. A detailed knowledge of the evolution of the wake is therefore required. Pursuant to this goal, this report introduces a new aerodynamic model, built into the open-source simulation suite QBlade Ocean (hereafter QB).

The model makes use of a hybrid Eulerian-Lagrangian formulation of the flow using vortex particles and is accelerated by applying the vortex-particle multilevel (VPML) method. The method is capable of simulating not only the flow in the near-wake of the turbine, but also the evolution of the far-wake. The method has been validated against an experimental turbine and comparable results using higher-order aerodynamic models. Numerous cases have been simulated which illustrate the applicability of the method to more complicated aerodynamic scenarios. The solver makes use of the graphical processor unit (GPU) to optimise calculations and significantly reduce the computation time of large aerodynamic problems.

1.   INTRODUCTION

The context within the FLOATECH Project is first outlined, followed by a brief overview of the structure of the report.

1.1.   CONTEXT WITHIN FLOATECH

This report summarises the work done in Task 1.1 of Work Package 1. This involves the development and implementation of the hybrid Eulerian-Lagrangian flow solver with the multilevel method and the coupling of this solver into QB. The purpose of the higher-order flow solver is to be able to simulate accurately and efficiently the macro-effects on the development of the turbine wake due to rotor motion and excitation. This is linked directly with the main objective of the FLOATECH project to improve simulation capabilities, particularly for the application to floating offshore turbines. Within the context of the FLOATECH project specifically, the ability of the solver to treat accurately the effects of wake excitation are directly applicable to the simulations carried out within WP3 and WP4. Within WP3, the motion of the turbine will be controlled through application of the feed forward wave-based control strategy. This motion will strongly couple the turbine wake with the acting aerodynamic loads. As these are a necessary input to the controller, the correct simulation of this coupled effect is paramount. Within WP4, active wake mixing will be employed in order to exploit a synergy between turbine motion and wake development. The qualitative development and breakdown of the wake must be accurately captured in order for quantitative efficacy metrics to be evaluated. This requires the application of a flow solver capable of treating higher-order physical effects.

1.2.   REPORT STRUCTURE

The current state-of-the-art of aerodynamics modelling of wind turbine wakes shall be described first in Section 2 in order to provide the conceptual background to the implemented method and a context within the spectrum of current simulation tools. The existing aerodynamic models within QB along with their respective strengths and limitations shall be described in Section 3. In Section 4 a description of the VPML solver shall be given. This includes the relevant field equations, the method of spatial integration, the resolved field quantities and important numerical parameters for the integration routines. The optimal scaling of the solver shall also be described along with a description of the applicable optimisations. In Section 5 important simulation parameters of the VPML solver will be investigated. Following this the solver will be validated against an experimental turbine and other solution methods. The applicability of the VPML solver within QB to the cases of interest within the FLOATECH project will be demonstrated in Section 7, these include the case of strong rotor motion for application to WP3 and to wake excitation for WP4. In Section 8 the conclusions of the report along with the outlook of the solver will be discussed.

2.   AERODYNAMIC MODELLING STATE-OF-THE-ART

The simulation of the aerodynamics of a wind turbine is a problem which, without the introduction of appropriate models, very quickly becomes overwhelmingly complicated. The main factor which gives rise to the high complexity is that the aerodynamics act over a range of spatial scales. These dimensions span multiple orders of magnitude, complicating numerical treatment. This is summarised in the table below:

Flow Object	Approx. Flow Length Scale	Approx. Flow Time Scale
Airfoil boundary layer	10^{-2} m	10^{-2} s
Airfoil section	1 m	10^{-1} s
Blade	10^1 m	1 s
Turbine & Wake	10^2 m	10^0 - 10^2 s
Farm	10^3 m	$> 10^2$ s

Table 1: Spatial and temporal time scales of the aerodynamics of a wind turbine.

Corresponding to the great range of length scales are naturally also diverse time scales. The resolution of these different scales with a single model places great restrictions on the fidelity of the solver. In practice, this challenge is commonly overcome by treating the very small scale flows (boundary layer-profile-blade) and the large scale flows (turbine-wake-farm) with separate aerodynamic models. These are discussed separately in the following sections.

2.1.   TREATMENT OF AIRFOIL & BLADE-SCALE FLOWS

The flow over the airfoil (quasi-2D) and blade (3D) of a wind turbine presents numerous modelling challenges due to the variation of length and time scales, the spatial and temporal variation of the inflow field and the effects of blade rotation. These can be divided simply into methods which resolve the blade surface and methods which avoid resolution of the blade surface. These are described separately below.

2.1.1. Blade-resolving methods.

In these methods the blade surface and the surrounding regions are resolved using a suitable mesh and the equations of flow are discretised on this mesh. Normal and shear stresses are integrated over the surface in order to calculate aerodynamic forcing. Assuming the vorticity of the inflow field to be small, the flow can be conceptually divided into two regions: the rotational boundary layer of the blade, which is dominated by viscous forces in the fluid and the irrotational or inviscid outer region, which is described by a potential flow. This is illustrated in Figure 1. The potential flow region can be resolved using a potential flow solver [1]. The boundary layer flow can be treated by coupling the potential flow solver to a suitable integral boundary layer solver [2,3,4,5]. These approaches avoid the resolution of the boundary layer normal to the profile and incur therewith relatively low computational expense. Alternatively, both

regions can be resolved with a blade-fitted mesh and the field equations can be numerically approximated on the mesh using either finite volume (FV) or finite difference (FD) methods [6]. A range of meshing options and solver types are available depending on the modelling approach. These methods generally fall under the standard rubric of computational fluid dynamics (CFD). This is illustrated for the volume mesh around a blade in Figure 1. These solution methods, although providing more insight into flow details and physics, are generally still too computationally expensive to be applied in design iterations of a wind turbine blade. Exceptions are made for investigation of specific flow phenomena or academic investigations.
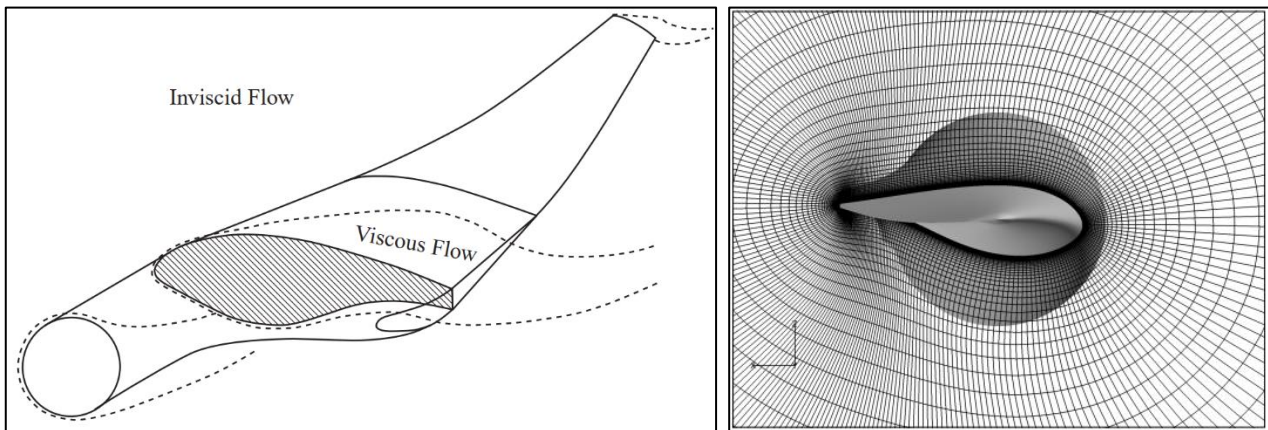

Figure 1: Flow regions around a wind turbine blade. Left: Separation of the inviscid and viscid regions [7]. Right: Volume mesh of a finite-volume solver of a turbine blade [8].

2.1.2. Blade-modelling methods.

A much more computationally efficient approach is to model the blade with a method which ensures conservation of global quantities and direct application of tabulated airfoil data. The blade element method allows for the expression of lift and drag forces on a spanwise section of the blade by treating each section as being locally quasi-2D. The local inflow velocity, angle of attack and sectional geometrical data is applied to determine, based on lift and drag coefficient look-up tables, the forces acting on a blade section [9]. These can be directly related to the circulation of the section by applying the Kutta-Joukowski theorem [10]. 3D aerodynamic effects such as tip induction can be accounted for in a number of ways. The lifting -line (LL) method is a computationally efficient approach which treats each lifting section as a vortex filament [11]. The influence of each blade filament on neighbouring sections is accounted for in the force calculation and effects, such as the influence root or tip vortex of the blade, are automatically accounted for [12]. This approach has the advantage that numerous corrections can be applied in order to account for blade sweep or dihedral [13], blade curvature [14], or parasitic drag [15]. Alternatively, 3D effects can also be accounted for within the realm of FD or FV methods by applying the actuator-line method [16]. The blade in this case is not resolved per se, however the blade region is resolved with a mesh and the lift and drag forces are introduced into the flow domain by means of a volume forcing term, again calculated from tabulated data. To avoid singularities the forcing is introduced over a finite volume by means of a convolution with an appropriate length scale [17, 18]. These two approaches are visualised in Figure 2.
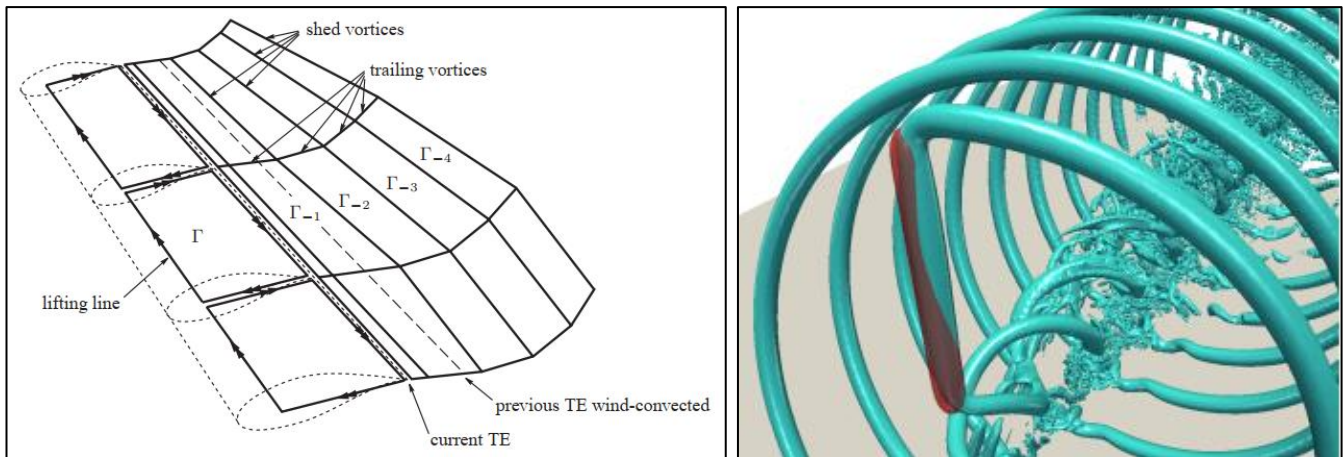
Figure 2: Treatment of 3D aerodynamic effects of a wind turbine blade. Left: Lifting line method [12]. Right: Actuator line method [17].

2.2.   TREATMENT OF TURBINE & WAKE-SCALE FLOWS

The flow in the wake of a wind turbine presents a range of modelling challenges due to the variation of length and time scales, the influence of environmental conditions, and the inherent instabilities present in the wake flow which give rise to wake breakdown and recovery [19]. Attention here is focused on simulation methods. For a detailed discussion of wake stability, the reader is referred to [20,21,22]. The modelling of a wind turbine wake can be broadly separated into three classes: low, medium and high-fidelity methods, in increasing order of resolution and computational expense. These three categories are described below.

2.2.1. Low-fidelity methods

These methods avoid resolution of the wake by making assumptions about the wake topography and/or circulation distribution. Actuator disc methods, developed within the framework of propeller theories, assume that the rotor acts as a loading body which imparts an instantaneous volume force to the fluid in the form of a pressure term. The entire flow through the turbine is considered to be a streamtube of the flow. Expressions relating the thrust force and the flow deceleration or induction can be derived under the assumption of an ideal fluid [9]. This can be extended to account for the rotation imparted to the stream by the turbine. This illustrated in Figure 3. These models only give a mean velocity in the wake and make no account of unsteady or 3D wake effects. Extensions which account for more realistic wake velocity profiles include the Jensen model [23,24] and Bastankah & Porte-Agel wake models [25,26]. An alternative approach is the treatment of the wake system with a vortex system. These include an analytical treatment of the wake system with the Joukowski or Betz rotors [27] and vortex cylinder treatments [28].

By discretizing the rotor plane into annular sections and ignoring interaction between streamtubes, the contribution due to each annulus can be individually treated in order to solve for the distribution of blade loading (and therewith wake induction) as a function of the radius. The approach can be combined with

the blade element method described in Section 2.1.2 in order to solver iteratively for the induction at each blade section. This is referred to as the blade-element momentum (BEM) method and is commonly applied for low fidelity, quick blade design. The underlying assumption of this method, such as steady inflow, streamtube independence and uniform inflow can be accounted for with correction models [27].
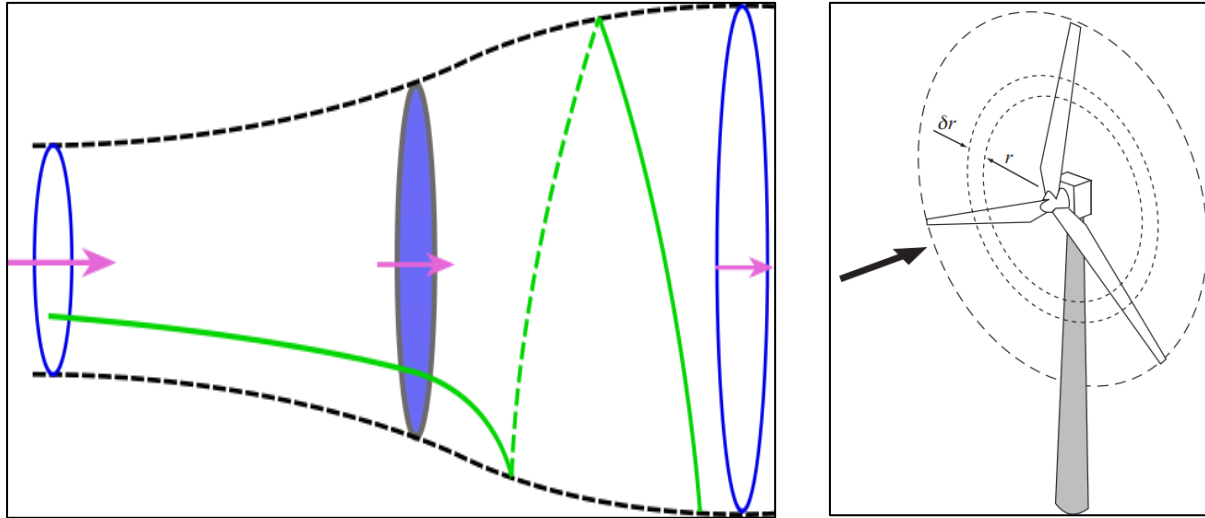

Figure 3: Left: Actuator disc representation of turbine. Inflow from left is decelerated through the rotor disc (shaded). Right: Annulus treatment of the rotor disc [9].

These methods, although carrying a very low computational expense, do not spatially or temporally resolve the wake and are therefore unsuitable for the intended applications of the FLOATECH project.

2.2.2. Medium-fidelity methods

These methods involve resolution of the wake flow, however without requiring a full FD or FV mesh of the volume. This includes the use of uniform template mesh. The simplest of these methods discretises the wake into a set of vortex filaments [12]. The velocity induced by the filaments can be analytically expressed for a straight filament, making calculation of the induced velocity in the wake computationally simple. Wake node end points are convected freely as Lagrangian markers, allowing the wake topology to freely evolve under self-influence. For this reason, the methods are referred to as Lagrangian methods. The use of filaments, by construction, implies that the vorticity field is inherently divergence free. These however rely upon the assumption of a potential flow, which quickly becomes unrealistic as viscous and turbulent shear stresses play a dominant role [29]. The inclusion of viscous stresses is allowed for by making use of vortex particles (VP) rather than vortex filaments [30]. In this case the particles are freely convected and their vorticity vector is updated according to the corresponding field equations. In this sense, the particles act practically as quadrature nodes for the vorticity field. The particle strength exchange scheme allows for viscous effects to be included, albeit at the cost of restrictive stability constraints [31]. Distortion of the Lagrangian grid gives rise to dense particle concentrations and unrealistic flow gradients, this is overcome by regularly remeshing the particles into a regular grid using moment-conserving mapping procedures [32,33].

When using the aforementioned methods calculation of the field quantities requires superposition of the influence of each flow element (filament or particle), evaluated at each element position. This problem scales as $O(N^2)$, where N refers to the number of flow elements. Methods for acceleration include truncating wake elements or combining wake elements [34], these approaches are however unsuitable when resolving wake flow phenomena. The computational expense of this problem can be reduced to $O(NlogN)$ by using appropriate spatial coarsening techniques, such as the Barnes-Hut algorithm [35]. A further improvement to $O(N)$ can be achieved by applying the Fast-Multipole Method (FMM), which combines spatial coarsening with approximating spherical harmonics for far-field interactions to ensure solution accuracy [36,37]. A similar technique, making use of spatial coarsening and a polynomial approximation, the multi-level multi-integration cluster (MLMIC) is based on a similar concept as the FMM, however conceptually simpler for application to standard integration kernels [1,38]. This method is illustrated in Figure 4.
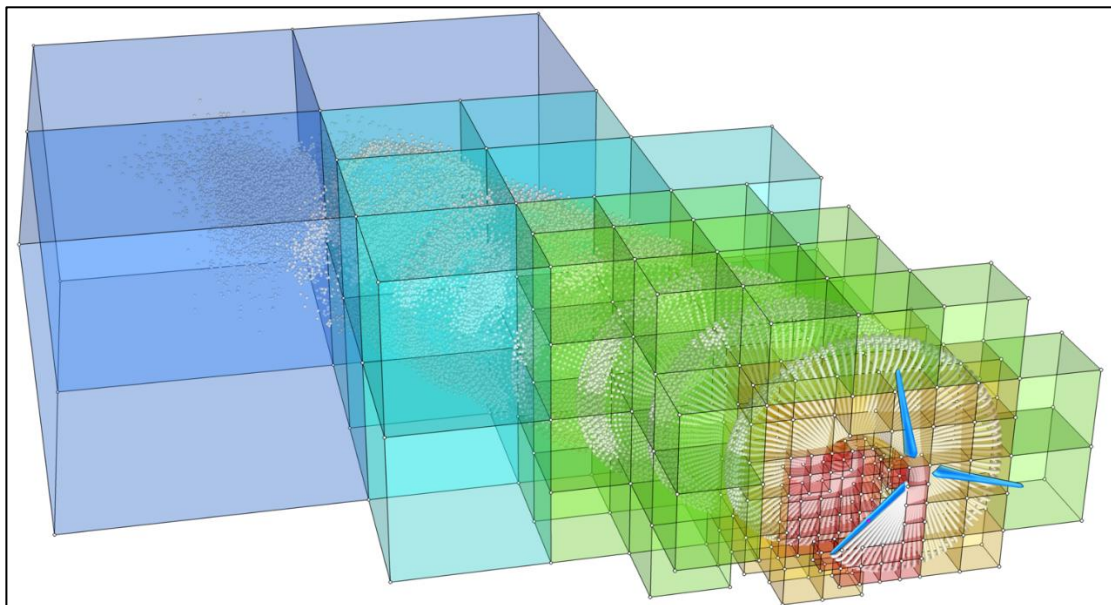
Figure 4: Spatial coarsening employed by the MLMIC method for the calculation of the evolution of Lagrangian wake markers of a yawed turbine [1].

An alternative approach to reducing computational expense is to solve the unknowns on a regular grid, and map the solution back to the Lagrangian markers. This style of approach is referred to as a hybrid Eulerian-Lagrangian method and allows the use of a Fast Poisson solver for the grid [32]. The Lattice-Boltzmann method is a further numerical method requiring the solution on a regular grid, which allows significant optimization with multi-processor configurations such as a GPU, as only near-field interactions between elements must be calculated [39].

2.2.3. High-fidelity methods

These methods (generally Eulerian) rely on a full discretization of the flow field. The Navier-Stokes equations are solved on the spatial mesh using FD or FV methods [16]. These methods are generally referred to in the greater community as CFD methods. A large, generally complicated mesh must be generated which is body-fitted and spatially irregular in order to ensure gradients are adequately

captured by the volume mesh [6] - see Figure 5. In order to avoid boundary reflections in the solution, meshes must be generated which are generally much larger than the simulated area of interest, greatly increasing the number of degrees of freedom (DOF) of the calculation and therewith computational expense. The advantage of such methods is the ability to extract higher order gradient information from the grid, which allows for the inclusion of turbulence models. For unsteady problems the most common approaches to the treatment of turbulent stresses are the unsteady Reynolds-average Navier-Stokes models (URANS) or large-eddy simulation (LES) [40]. A range of options exists regarding time integration, finite difference accuracy and turbulence models.
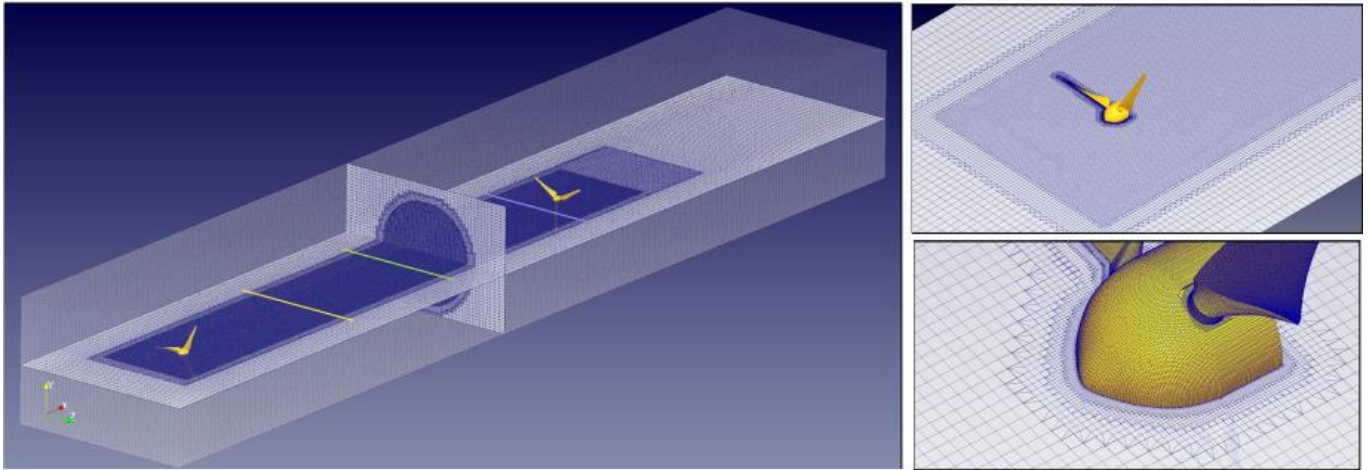

Figure 5: Mesh for FV treatment of a wind turbine wake with CFD [41].

These methods provide the greatest insight into the flow phenomena in the wake, for which reason they have found great application within the research community. The necessity to generate a tailored mesh for each turbine geometry, combined with the greater computational expense make them however unsuitable for practical application within an iterative design environment. For these reasons, it has been concluded that the most ideal solution for application within QB is the development of an advanced medium-order method. This is further described in Section 4.

3.   EXISTING AERODYNAMIC MODELS WITHIN QBLADE OCEAN

It is instructive to describe the aerodynamic modules which are currently implemented within QB. These modules have been partially utilised in the implementation of the new VPML solver. Their description here is therefore practical for the validation section.

3.1.   TREATMENT OF AIRFOIL AND BLADE

QB allows for the import of arbitrary airfoil contours for the turbine blade aerodynamic specification. These profiles can then be analyzed with the XFoil software (see Section 2.1.1) in order to generate lift and drag polars for a given range of angles of attack (AoA) at single or multiple Reynolds numbers [2]. Alternatively, the polars can be imported from an external file. As lift coefficients are required for all possible AoA values, these can be extrapolated with the 360° polar module using either Montgomerie or Viterna extrapolation [34]. A screenshot of the associated module is given in Figure 6. In addition to the

specification of airfoil coefficients, attached and detached coefficients and attachment function values for application with the featured dynamic stall models can be specified [42,43].
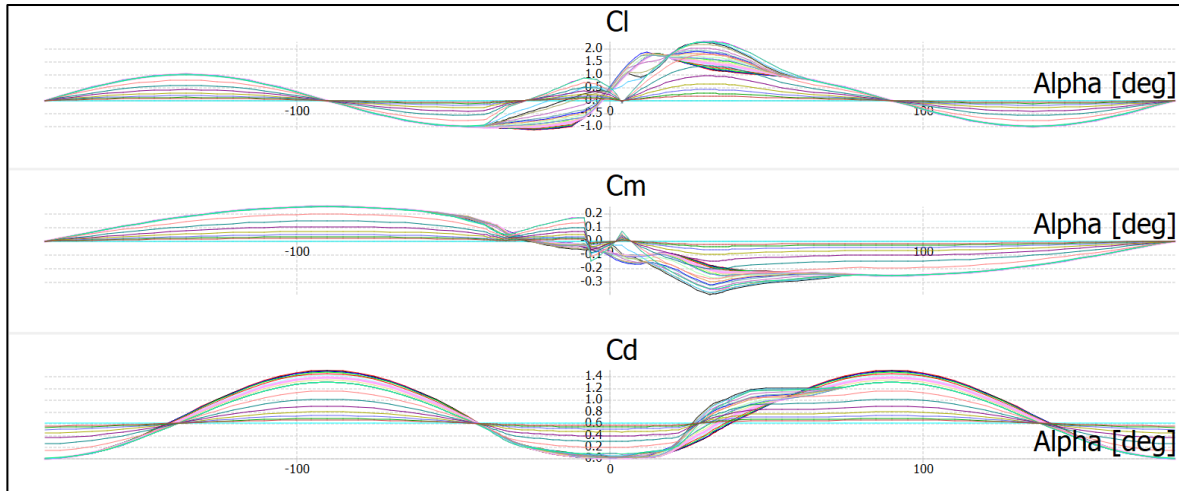

Figure 6: Polar extrapolation module in QBlade Ocean.

With a catalogue of airfoil profiles and their corresponding aerodynamic coefficients, the (HAWT) rotor blade design module can be used to create the blade geometry for the simulation. This allows the specification of multiple turbine blade sections as a function of radial position, chord length and blade twist. For each blade section a corresponding profile is assigned, along with either a single or multiple (Reynolds number) airfoil polars. This information is used in the aerodynamic analysis in order to specify local blade geometry and aerodynamic coefficients.

3.2.   AERODYNAMIC MODEL: UNSTEADY BEM

For simulations where the assumptions of the BEM model are valid, an unsteady BEM version is available. This is implemented following the description in [44] which makes use of an azimuthal grid treatment of the individual radial and azimuthal streamtubes. Corrections for tip loss and yaw are included along with unsteady effects through the use of indicial functions. The stored blade aerodynamic data defined in the aerodynamic and blade definition are applied here in the iterative solver for the sectional induction factors.

3.3.   AERODYNAMIC MODEL: LIFTING LINE FREE VORTEX WAKE

The vortex filament method described in Section 2.2.2 has also been implemented within the Lifting Line Free Vortex Wake (LLFVW) module [34,12]. The velocity at each blade section is calculated as the sum of the inflow field, relative velocity and induced velocity from wake elements. At each time step, the circulation at each blade section is iteratively determined from the Kutta-Joukowksi theory by making use of the stored blade sectional aerodynamic data [12]. The spatial variation in circulation is passed into the wake as trailing vorticity and the temporal variation of circulation is passed into the wake as shed vorticity. The wake consists of shed and trailing wake filaments as illustrated in Figure 7. Connectivity between these is guaranteed by wake nodes, which are convected as Lagrangian flow elements. The velocity

induced by the filaments makes use of a van-Garrel style vortex core model [12]. The filament initial core size, growth rate and maximum stretching are all specified during initialization of a simulation.
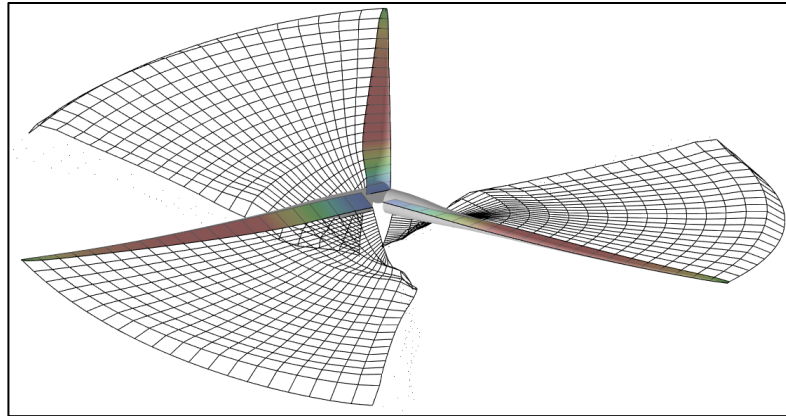

Figure 7: Shed and trailing wake filaments when applying the LLFVW model.

This module is extensively used in the aerodynamic model introduced in this report and module features shall be detailed in the following sections.

4. HYBRID EULERIAN-LAGRANGIAN AERODYNAMIC MODEL

As part of WP1 of the FLOATECH project, an advanced aerodynamic model has been implemented into QB. Advanced in this sense refers to the ability of the model to resolve physical flow quantities and flow features which are not resolved by the LLFVW model. The purpose of this is to enable the simulation of more complicated wake phenomena, such as wake breakdown and recovery within a medium-order framework without the necessity to resort to high-performance computing (HPC). It is desired to make use of an adaptive grid, such that only regions containing vorticity need to be resolved. For this reason, it has been chosen to proceed with a Lagrangian method. The VP method has been chosen as this allows for the treatment of higher order effects such as vortex stretching and viscosity. The unfavorable scaling requires the implementation of an acceleration technique in order to improve computational efficiency. For this purpose, the MLMIC method (see Section 2.2.2) has been adapted for the treatment of vortex particles. The underlying equations of the model are first described, followed by a description of the vortex particle method. The multilevel integration scheme is then described, including implementation details and simulation parameters.

4.1. FIELD EQUATIONS

It shall be assumed that the flow of an incompressible fluid is being modelled. The vorticity field $\vec{\omega}$ can then be shown to be solenoidal:

$$\vec{\omega} = \nabla \times \vec{u} \qquad \rightarrow \qquad \nabla \cdot \vec{\omega} = \nabla \cdot (\nabla \times \vec{u}) = \vec{0}, \tag{1}$$

where $\vec{u}$ is the velocity of the flow field. Assuming that body forces acting on the fluid are irrotational, taking the curl of the Navier-Stokes equations gives the vorticity transport equation (VTE):

$$\frac{d\vec{\omega}}{dt} = \frac{\partial \vec{\omega}}{\partial t} + (\vec{u} \cdot \nabla)\vec{\omega} = (\vec{\omega} \cdot \nabla)\vec{u} + \nu \nabla^2 \vec{\omega}. \tag{2}$$

This equation expresses conservation of momentum of the fluid and shall be applied in the calculation of the particle strength evolution. The Helmholtz equation demonstrates that any twice continuously-differentiable vector field (here taken to be the velocity field) can be expressed as the sum of an irrotational scalar potential ϕ and a divergence-free vector potential ψ (hereafter referred to as the stream function):

$$\vec{u} = -\nabla\Phi + \nabla \times \vec{\psi} = \vec{U}_\infty + \nabla \times \vec{\psi}, \tag{3}$$

where $\vec{U}_\infty$ can be considered a potential flow field. Taking the curl of this equation gives the Poisson equation, which directly relates the stream function and the vorticity field:

$$\nabla^2 \vec{\psi} = -\vec{\omega}. \tag{4}$$

The solution to this equation lies at the core of the calculation method applied in the VPML solver.

4.2. VORTEX PARTICLE METHOD

As seen in Eq. (4), knowledge of the vorticity field is required for the solution to the Poisson equation. In the VP method this is achieved by representing the vorticity field as a set of vorticity-carrying particles:

$$\vec{\omega}(\vec{x}) = \sum_p \vec{\omega}_p \, \delta(\vec{x} - \vec{x}_p), \tag{5}$$

where $\vec{x}$ is the evaluation position (probe), $\vec{x}_p$ is the particle position (source), $\vec{\omega}_p$ is the vorticity vector of the particle and δ is the Kronecker delta.

4.2.1. Greens functions for the Poisson equation

The solution to the Poisson equation (4) for the stream function is given by applying the Green's function for the Laplacian in an unbounded domain:

$$\vec{\psi}_p(\vec{x}) = -\frac{1}{4\pi} \frac{1}{|\vec{x} - \vec{x}_p|}. \tag{6}$$

The solution due to a continuous distribution of vorticity sources is then given as:

$$\vec{\psi}(\vec{x}) = \int_V -\frac{1}{4\pi} \frac{1}{|\vec{x} - \vec{x}_p|} \vec{\omega}(\vec{x}) \, dV = G * \vec{\omega}, \tag{7}$$

where $*$ is the convolution operator. The equivalent expression for the discrete vortex particle method is given by :

$$\vec{\psi}(\vec{x}) = \sum_N -\frac{1}{4\pi} \frac{\vec{\omega}_p}{|\vec{x} - \vec{x}_p|} dV, \tag{8}$$

where dV represents the volume occupied by the particle. As can be seen, this function becomes singular for points where $\vec{x} = \vec{x}_p$ when applying a singular particle treatment. This can be overcome by specifying a regularisation function which effectively distributes the vorticity of the particle in a localised region, removing the singularity of Eq. (8). This can be carried out either in real space or in the Fourier space [45]. This regularisation is inherently handled by the near-field treatment of the method employed here and is described further in Section 4.4.1.

4.2.2. Particle evolution

Evolution of the particle position is treated in a Lagrangian sense by directly applying the convective derivative at the particle positions:

$$\frac{d\vec{x}_p}{dt} = \vec{u}(\vec{x}_p). \tag{9}$$

Evolution of the particle strength is achieved by solving the vorticity transport equation (2) at the particle positions:

$$\frac{d\vec{\omega}_p}{dt} = (\vec{\omega} \cdot \nabla)\vec{u} + \nu \nabla^2 \vec{\omega}. \tag{10}$$

The first term on the right-hand side of this equation is the shearing or stretching of the vorticity field due to the velocity gradient. The second term is the contribution of viscous stress to the shearing field, where ν is the kinematic viscosity of the fluid. Within the VPML solver the stream field is resolved, based on this the field quantities required in the above equations are resolved. This will be detailed in later sections.

4.3. MULTILEVEL METHOD

As described in the previous section, the solution of the stream function field requires the convolution of the source vorticity field. Calculating Eq. (7) for N particle positions is a problem which, due to the influence of N particles, has a computational expense which scales as O (N²) (as described in Section 2.2.2). This would in practice place a severe restriction on the allowable resolution of the field, limiting the accuracy of the wake simulations. To overcome this bottleneck, the MLMIC method has been applied to the solution of the unbounded Poisson equation. Key to the functioning of the MLMIC method is the concept of separating near-field and far-field interactions. This is described first, followed by the description of methods which allows the reduction of the computational expense to O(N). In this report the main concepts are illustrated, for a detailed description of the MLMIC method the reader is referred to [1,38,46].

4.3.1. Separation of near-field and far-field influences

A key concept of the MLMIC method is the spatial segregation of the convolution regions in Eq. (7). The near-field and far-field of a given evaluation position is separated into regions such that:

Near field: $\quad x_i - x_p \leq d_{NF}$

Far field: $\qquad x_i - x_p \geq d_{NF},$

for some suitable Cartesian distance d_{NF}. This is accomplished by binning source particles and receiver positions into boxes B of length h. A box containing source particles (vorticity particles) is designated with B^J. A box containing receiver (probe) positions is designated with B^I. The problem of evaluating the convolution of Eq. (7) is now conceptually no longer the calculation of the influence of source points on probe points, but rather the calculation of source boxes on probe boxes. This concept is illustrated in Figure 8 for a 2D case for simplicity. The influence of source boxes on probe points is not calculated directly using Eq. (7). Instead, the interaction is calculated between a grid node template within each box. These are described in the following section.
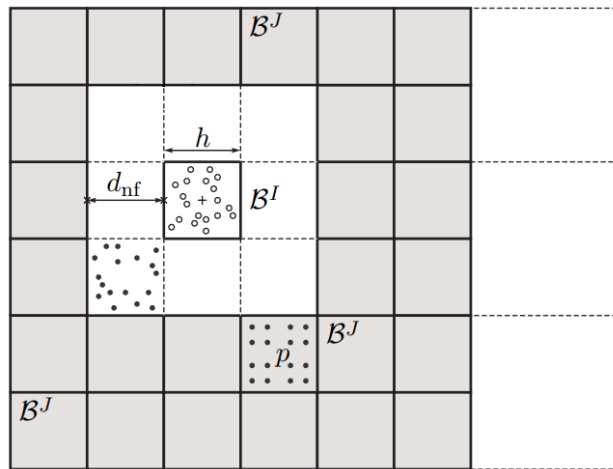

Figure 8: Separation of space around a region (Box B^I) into near-field and far-field. Image taken from [1]. The receiver box B^I contains probe points, where the field quantities are desired to be calculated. The surrounding source boxes B^J contain source nodes.

4.3.2. Far-field interactions: Grid nodes for interpolation and anterpolation

All far-field interactions are calculated not between sources particles and probe points, but rather between source nodes (within B^J) and receiver nodes (within B^I). The solution at the receiver nodes is then interpolated to the actual probe positions. The interpolation function and nodes are chosen in order to minimise the interpolation error and ensure a smooth interpolant. Following the method described in van Garrel [1], barycentric Lagrangian interpolation is used. The optimal interpolation node placement for this type of interpolation is given by the zeros of the Chebyshev polynomials [47]. The order p of this polynomial interpolation is user-specified and dictates the order of accuracy of the interpolation, along with the number of interpolation nodes. As an illustration, the positions of the interpolation nodes for the case $P = 4$ are shown for a source box in Figure 8.

An inverse procedure is used to approximate the kernel function at the source nodes within B^J. In this case one refers to the adjoint interpolation or **an**terpolation. The procedure is fundamentally similar as with the receiver nodes. In this case though, the transpose interpolation is carried out. These procedures are illustrated in Figure 9. As the number of interactions between boxes scales as P^3, the computational expense increases with increasing polynomial accuracy.
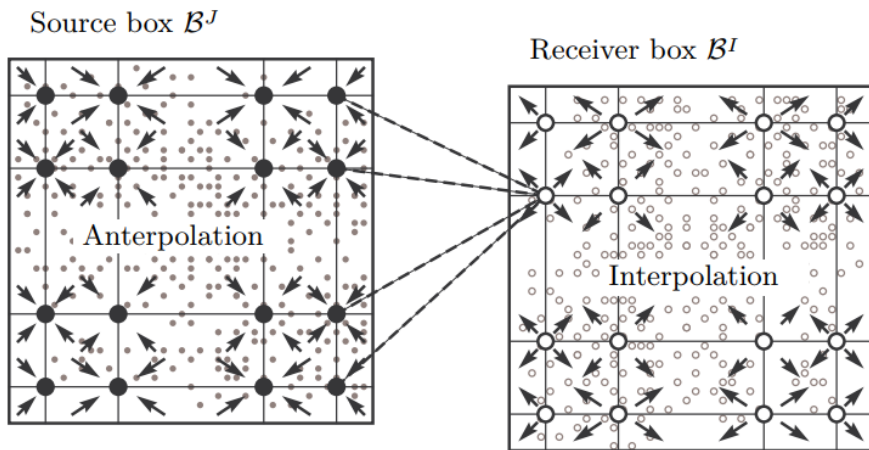
Figure 9: Interaction between source and probe boxes for the case P=4. Left: Source anterpolation for a source box. Right: Interpolation for a receiver box. Image taken from [1].

4.3.3. Spatial coarsening

The geometric symmetry between source nodes and receiver nodes for a given source-probe box pair is exploited by making use of interaction templates which can be calculated for the given kernel (in the case of VPML, the stream function kernel) at the beginning of the simulation. This alone achieves a computational advantage as compared to the direct particle-probe calculation. The considerable further reduction of the computational expense to $O(N)$ is achieved by applying spatial coarsening. The source distribution and influence are approximated on progressively coarser grids, depending on interaction distance. Source anterpolation and influence interpolation between two grid levels is illustrated in Figure 10. In this sense it can be seen how the computational expense of the integration is greatly reduced, as the polynomial approximation of the influence is progressively coarsened based on the separation distance between source and probe positions.

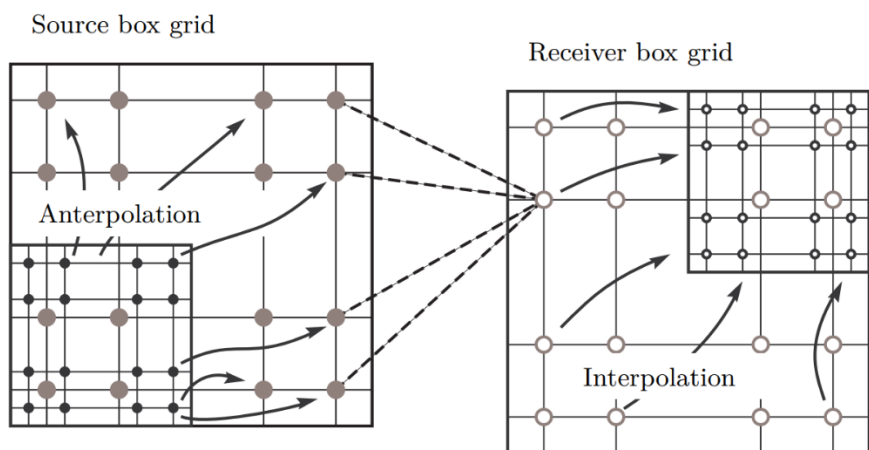**Figure 10: Source anterpolation and influence interpolation between two grid levels. Image taken from [1].**

The asymptotic nature of the given kernels ensures that the error of this approximation is controlled purely by the order of interpolation P. This was investigated for the stream function kernel and it was shown in [46] that the integration error scales logarithmically with P. The interaction templates,

depending on the kernel can be calculated for every grid level. In the case of the stream function kernel, they are simply multiplied by a constant scaling factor.

4.4.   VORTEX PARTICLE-MULTILEVEL METHOD

It will be described in the following sections how the MLMIC method has been applied to the vortex particle problem with the VPML solver, along with the methods used to extract the necessary field quantities for particle evolution. It is important to note at this stage that the MLMIC integration has been applied to integrate the convolution of the stream function given by Eq. (7).

4.4.1. Calculation of near-field influence

A range of options exists for the calculation the near-field influence of neighbouring source and probe boxes. One approach is to apply directly regularised particle kernels [30]. A fast Poisson solver can also be applied to the solution on an underlying grid, followed by application of the James-Lackner algorithm to calculate boundary interactions [46]. A somewhat simpler methodology has been applied within the VPML solver. The sources within a source box B^J are mapped to an underlying regular grid of cell size H using a suitable moment-preserving mapping function [31]. The influence of these points on the equivalent regular probe grids of the neighbouring boxes are calculated. This interaction can also be calculated during preprocessing due to the symmetry of each source-probe box pair. This is illustrated in Figure 11 for a source box and its near-field. The size of the stencil grid is a function of the mapping procedure used and generally overlaps with the neighbouring boxes.
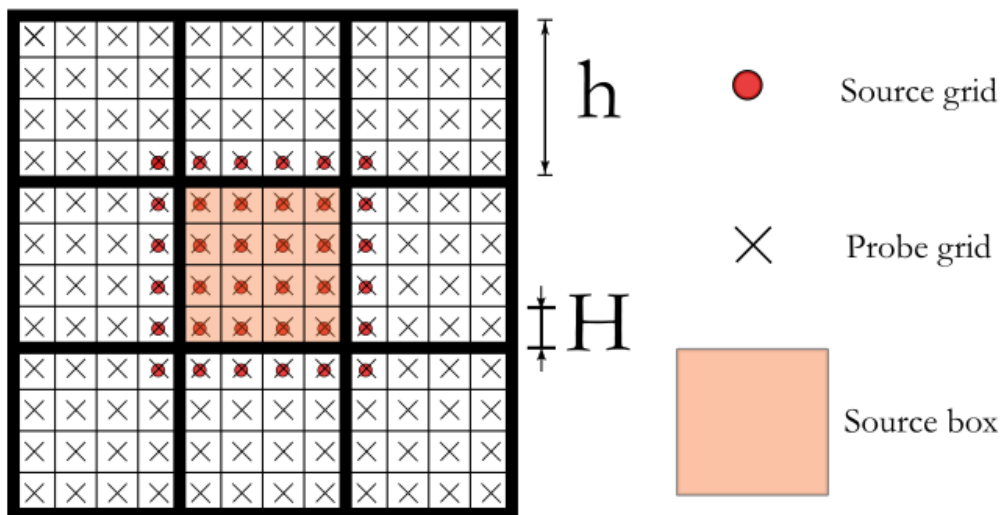
Figure 11: Near-field calculation within the VPML solver. The sources within the source box are mapped to an underlying grid and the influence of these source points on the surrounding probe grid are calculated.

A range of regularised Greens functions can be applied to this near-field interaction, in the work carried out in this report, the spectrally-convergent regularisation of Hejlesen has been applied [48]. This type of influence has the advantage that the regularisation parameter is specified by the grid size, thus avoiding the necessity of an additional modelling parameter.

4.4.2. Calculation of far-field influence

The method of Section 4.3.2 has been applied whereby the source kernel is anterpolated to the source nodes through the use of barycentric Lagrangian interpolation. In practice, it has been found to be more efficient to map the particle strength to an underlying grid, as is done for the near-field interaction, and then apply a template anterpolation matrix (calculated in pre-processing) to specify the source strengths of the anterpolation nodes. For the VPML model, the sources which are interpolated are given by the equivalent integral of the vorticity over the given area or the circulation of the particle. The interaction templates are calculated based upon the assumption that the far-field interaction behaves as a singular particle - Eq. (8). This assumption is acceptable, provided the minimum box size has been chosen to be sufficiently large [46].

4.4.3. Calculation of field quantities

As described previously, the stream function is calculated within the VPML solver. The influence is calculated at the probe grid points within each probe box as the sum of the near-field and far-field influences, see Figure 11. This is allowable due to the linearity of the Poisson equation. The solution to the stream function being known on the (regular) probe grid, finite differences are applied to calculate the desired flow quantities on the probe grid. The results are then mapped to the probe positions applying the same mapping procedure as was carried out for the source mapping. The individual components are described below.

4.4.3.1.   Velocity field

It can be seen from the Helmholtz equation (3) that the velocity can be calculated as the cross product of the stream function. The partial derivatives of the stream function are hence calculated on the grid and the free stream velocity is added in order to specify the total velocity field.

4.4.3.2.   Vortex stretching Field

Upon calculation of the velocity field on the grid, the same FD stencil can be applied to calculate the velocity gradient tensor. This is used together with the known vorticity on the grid (this was mapped for the near-field calculation- Section 4.4.1) to calculate the shear terms. Two expressions can be used for the calculation of this term:

$$\frac{d\vec{\omega}}{dt}_{shear} = \vec{\omega} \cdot \nabla \vec{u} \qquad \text{Non-conservative form} \qquad (11)$$

$$= \nabla \cdot (u\omega) \qquad \text{Conservative form} \qquad (12)$$

In the case of the conservative form, the product $u\omega$ is a second-order tensor. It was found during testing that the conservative form greatly improved the stability of solver, in agreement with the findings of Cocle et al. [32]. This was therefore applied in all cases simulated in this report.

4.4.3.3.   Viscous terms

The effect of viscous terms on the evolution of the particle set is accounted for by calculating the Laplacian of the vorticity field. The vorticity having already been mapped to the probe grid during the near-field step, it remains simply to apply a suitable FD stencil for the Laplacian. Following Cocle [32], an isotropic FD stencil is applied such that the solution is not sensitive to the orientation of the grid [49].

4.4.4. Particle set remeshing

As a particle set evolves in time, the combined effect of convection and stretching gives rise to a significant distortion of the Lagrangian mesh. If left unchecked, this leads a to region of strong particle concentration, which furthermore leads to greater distortion and instability of the solution. This can be overcome by applying particle set remeshing, where the particles are mapped to a regular grid in such a way that the moments of vorticity are conserved. This is illustrated in Figure 12. A range of mapping functions are available, depending on the order of the vorticity moments to be conserved [50].
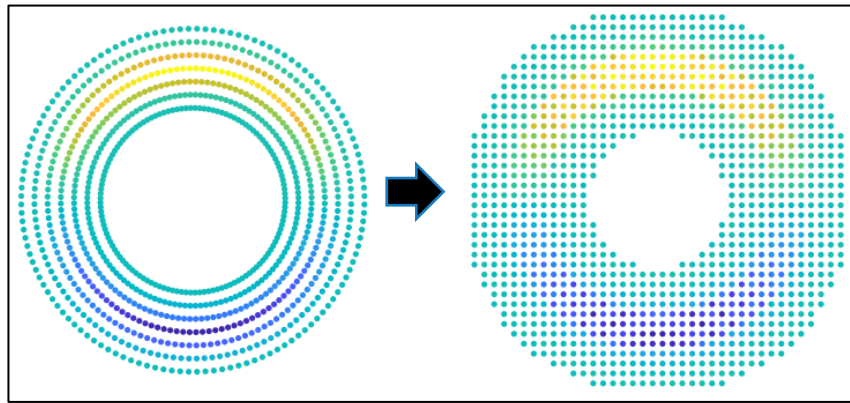

Figure 12: Particle set remeshing onto a regular grid.

An additional advantage of the remeshing procedure is that it practically introduces a mechanism which allows for viscous diffusion of the vorticity field by introducing new particles which allow the vorticity distribution to spatially expand. The frequency with which remeshing is applied is a simulation parameter.

4.4.5. Magnitude filtering

Left unchecked, the particle count will grow without limit each time particle remeshing is carried out due to the spatial expansion of the vorticity field at boundary regions - see Figure 12. This process has the advantage that it numerically approximates viscous diffusion. However, it greatly increases the number of particles in the simulation and thus increases computational time. An approach to limiting the size of the particle set is to employ magnitude filtering. The particle set is first scanned to determine the maximum particle strength $\vec{\omega}_{max}$. Following this, all particles are removed from the particle set for which $|\vec{\omega}| \leq F|\vec{\omega}_{max}|$, where F is referred to as the magnitude filtering factor. Clearly this approach is nonphysical as vorticity is removed from the particle set. A heuristic argument however can be made as $F \rightarrow 0$, the influence of the removed particles becomes vanishingly small. Approaches exist for compensating for the decremented global values [32], this however has not been applied in the work here.

5.   VPML SOLVER SENSITIVITY STUDY

A range of simulations have been carried out in order to assess the influence the main VPML solver parameters on the stability of the solution, dominant factors in the accuracy of the solution and practical limits for application to general cases. These parameters have been investigated in order to provide a foundation for the discussions in Section 6. The turbine geometry for the simulations carried out in this section is the MEXICO rotor geometry, described in detail in Section 6.2.2.

5.1.   BASELINE PARAMETERS

For each simulation carried out, a range of baseline parameters have been specified in order to simplify the analysis. These parameters have been deemed to be non-dominant with regards to the solution. It is assumed that their influence on the results is not critical. In cases where this may be the case, the value of the parameter which leads to higher accuracy has been chosen. These parameters are described below:

Blade discretization: Within the blade element module of QB, the blade discretisation in spanwise direction is a user-defined variable. The unmodified blade sectional information (see Section 6.2.2) would inevitably lead to spurious jumps in the blade circulation distribution and inconsistencies in the aerodynamic description of the near wake. For this reason, the blade elements have been discretised with a cosine spacing distribution with 20 blade elements. This resolution is sufficient for the solver fidelities investigated in this report. It is noted that for higher resolutions a finer resolution may be required.

Time integration scheme: The use of a simple 1st-order Eulerian time integration scheme has been demonstrated to give rise to less stable flow solutions using vortex particle methods [31]. For the integration of wake node, particle positions, and particle strengths a 2nd-order predictor-corrector scheme has been utilised.
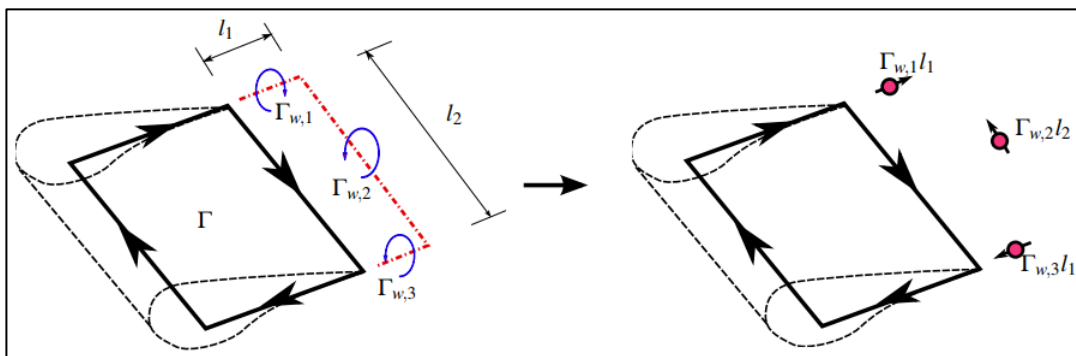
Figure 13: Conversion of the first wake filament into a particle ($N_F = 1$). In general, the elements are converted after a number of time steps.

Wake near-field specification: The application of the VP method requires a regularisation scheme. This has been shown to somewhat dampen the velocities induced in the near-wake of the blade [51]. For this reason, the blade near-wake has been discretised with a vortex filament method. In this region the predominantly high-Re flow is likely well captured by an inviscid method. After a given number of time steps N_F, the filaments are converted to particles which then provide the Lagrangian description of the

vorticity field of the VPML solver- this process is illustrated in Figure 14. By converting to filaments relatively quickly, strong interactions between the vortex particle and vortex filament treatment is avoided. The treatment of the regularisation function in both methods is significantly different, and allowing strong interactions between the two treatments can lead to inconsistencies in the flow field. In the simulations carried out here, $N_F = 20$. This case is illustrated in Figure 14.
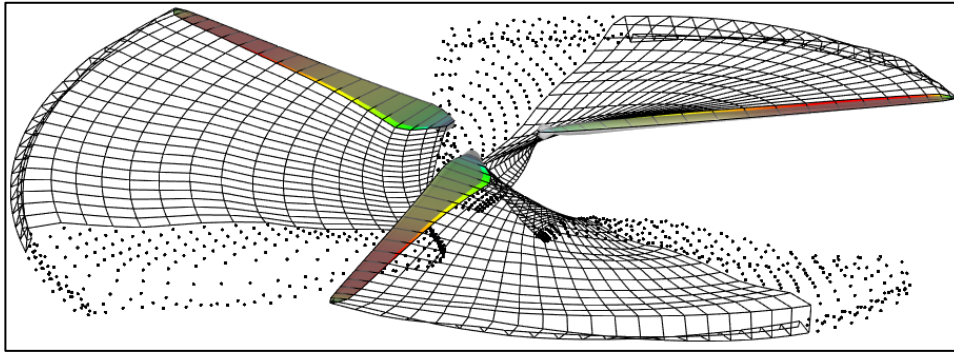

Figure 14: Conversion from filaments to particle in the blade near-field. Transitioning to a particle description quickly avoid numerical issues associated with the filament and particle regularisation.

Azimuthal discretisation: It has been found that a practical measure for the specification of the time-integration step size is the azimuthal angle subtended by the rotor $\Delta\varphi$ rotation during a time step. This factor directly influences the discrete filament treatment of the blade-near wake and therewith the immediate wake induced velocities in the rotor plane. A detailed discussion of the influence of this parameter is given in [51]. This parameter has relatively little impact on the wake dynamics as calculated by the VPML model as the particles are eventually mapped to the uniform grid during the remeshing procedure. For the simulations here, the azimuthal discretisation has been chosen as $\Delta\varphi = 3°$. The time-integration step size is then directly calculated for a given rotational speed of the turbine.

VPML Parameter- Particle mapping procedure: During an integration time step and during particle set remeshing, the particle must be mapped to the underlying regular grid in such a way that the moments of vorticity are conserved. There are a range of mapping procedures which are available. In order to ensure accuracy while reducing computational expense, the M_4' scheme has been applied in the work here [50]. This scheme ensures that 0th-2nd moments of vorticity are conserved for any mapping. Lower or higher order schemes may be applied, these however are not investigated in this work.

VPML Parameter- Near-field critical distance: The region around a given source or probe box which is considered to within the near or far-field is dictated by the parameter d_{NF} as illustrated in Figure 8. For the work here $d_{NF} = 1$ has been chosen, implying that the near-field of any box is composed of the box itself, plus its direct neighbouring boxes. It was shown in [46] that this specification is optimal for the stream function kernel, provided the base box size is adequately chosen. This shall now be described.

VPML Parameter- Base box size: The length of the base boxes h is chosen to be an integer multiple of the grid size H_{grid}. The specification of this influences directly, in combination with the d_{NF} parameter, the region of near-field influence of any probe box. This is therefore a function of the kernel which is being

integrated. It was demonstrated that $h = 8H_{grid}$ yields acceptable results for the spatial convolution of the stream function kernel with the MLMIC method in [46]. This has also been applied here.

VPML Parameter- Finite-difference order: As described in Section 4.4.3, the field quantities are being calculated through the application of finite differences on the regular grid. Broadly speaking, the higher order the scheme, the higher the computational expense of this step. In the simulations carried out in this report, the velocity and stretching fields are calculated using a 4th-order central-FD scheme and the viscous stretching is calculated with an isotropic 2nd-order Laplacian FD scheme [49].

5.2.   INFLUENCE OF GRID SIZE

The grid size H_{grid} determines practically the resolution of the solution field, and hence also the size of the base boxes. In this sense, an overly course mesh (large H_{grid}) can be expected to reduce the resolution and of the simulation. This resolution is furthermore the particle spacing after remeshing and therefore has a direct influence on how the remeshing procedure influences the vorticity distribution. The grid size was normalised with respect to the rotor diameter D and the results for $D/10$, $D/20$, $D/30$, and $D/40$ are shown in Figure 15.
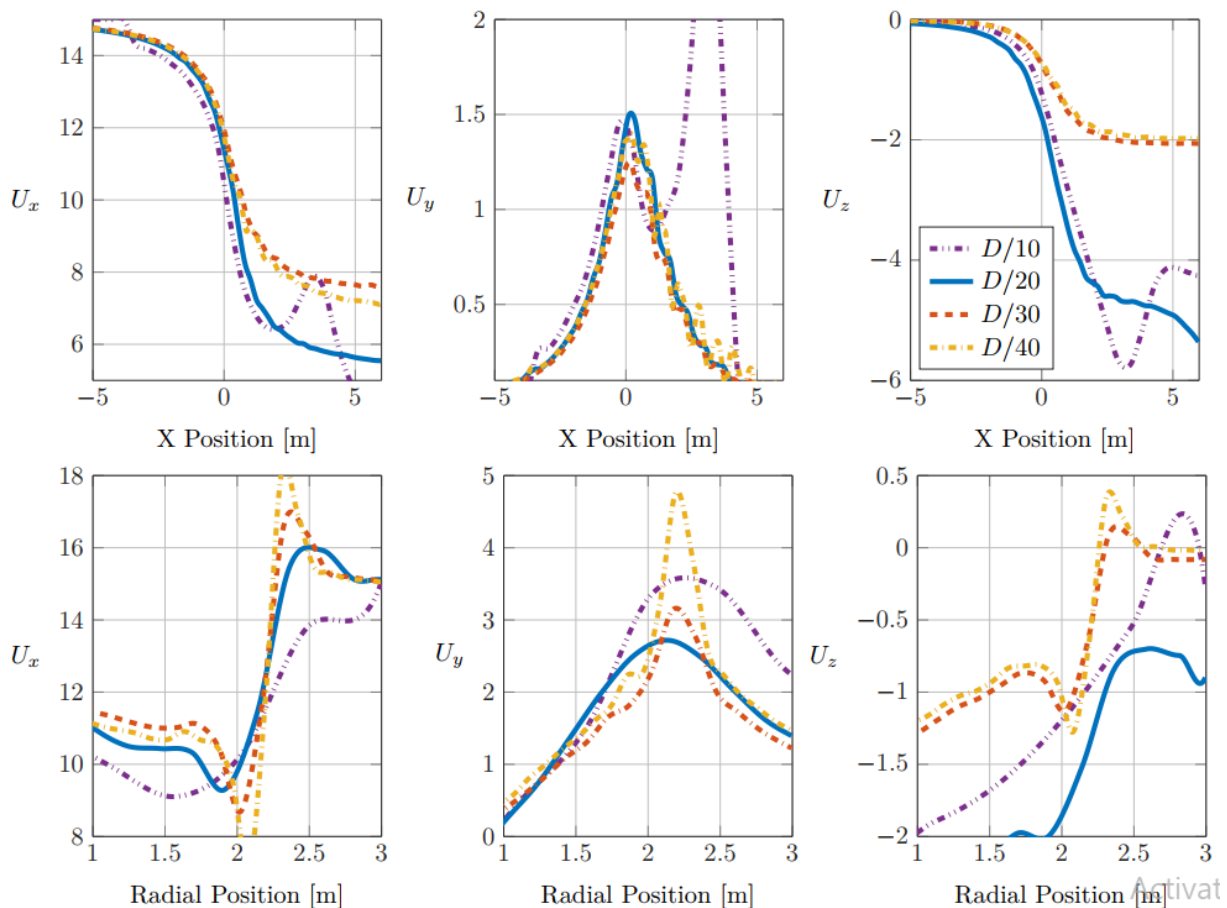

Figure 15: Axial (left), radial (centre), and tangential (right) wake velocities as a function of grid size. Top: Outer axial traverse. Bottom: Downstream radial traverse.

Numerous observations can be made here regarding the choice of grid size. The choice $D/10$ is seen to produce large deviations when inspecting the axial induced velocity in the near wake. It was observed that the stretching term is unstable for this grid size and a divergent interaction occurs between the starting vortex and the root vortex of the turbine which creates the erroneous velocities seen here. As discussed in [46], the majority of the stretching interaction occurs at small distances due to the nature of the velocity (Biot-Savart) kernel, a direct product of the stream function kernel. As such, at large grid sizes these effects are not accurately resolved. It is therefore recommended that for a choice of large grid size, the stretching term be deactivated. This was found to remove this effect. However, this will naturally have an influence on the accuracy of the solution as an important physical process is neglected.

It is observed that for resolutions finer than $D/30$ the results begin to converge. Finer resolutions were investigated but no difference was observed as compared to the $D/40$ case. As the main goal of the VPML model is to strike a balance between accuracy and computational time, for the simulations in this report a mesh resolution of $D/40$ has been chosen unless otherwise stated.

5.3. INFLUENCE OF POLYNOMIAL ORDER OF MLMIC SOLVER

The accuracy of the far-field convolution carried out within the MLMIC solver is a direct function of the polynomial order P of the kernel and influence scheme . It has been demonstrated that the error of integration is proportional to $\log P$ [1, 46]. It is therefore expected that increasing P will improve the simulation accuracy. This however is only one step in the calculation procedure and it remains to be seen what effect this parameter has for a practical application case. In order to resolve the stream function within the VPML solver, P must not be smaller than 2. Within [46] the value $P = 5$ was chosen for high fidelity simulations. The result of simulating the turbine wake with values of P within this range is shown in Figure 16.

It is observed that for $P>2$, the results are practically identical. This suggests that in this particular case, the polynomial order is not contributing significantly to the error, but rather that other factors influence the results more greatly. In cases where this may however not be the case, it is practical at this stage to inspect the computation time as a function of P. This is shown for the four simulated cases in Figure 17. Two important points must be considered before analysing this data. The first is that the predictor-corrector scheme is being applied in the time integration, which implies the solver is in fact being executed twice per time step. The second is that the time shown is composed not only of the convolution within VPML, but also of other computational steps including the system update steps and near field filament calculations. Keeping these points in mind, two points become clear when inspecting this data. The first is that the linear scaling of the problem with problem size N is very clearly observed for all values of P. This is a demonstration of the efficacy of the VPML solver and the $O(N)$ scaling. The second point is that the computation time is not significantly increased when using a greater polynomial order, suggesting that the the far-field integration is not the most computationally demanding step of the integration. A detailed analysis of this is out of scope and shall be detailed in further work. This agrees however with the results in [46].
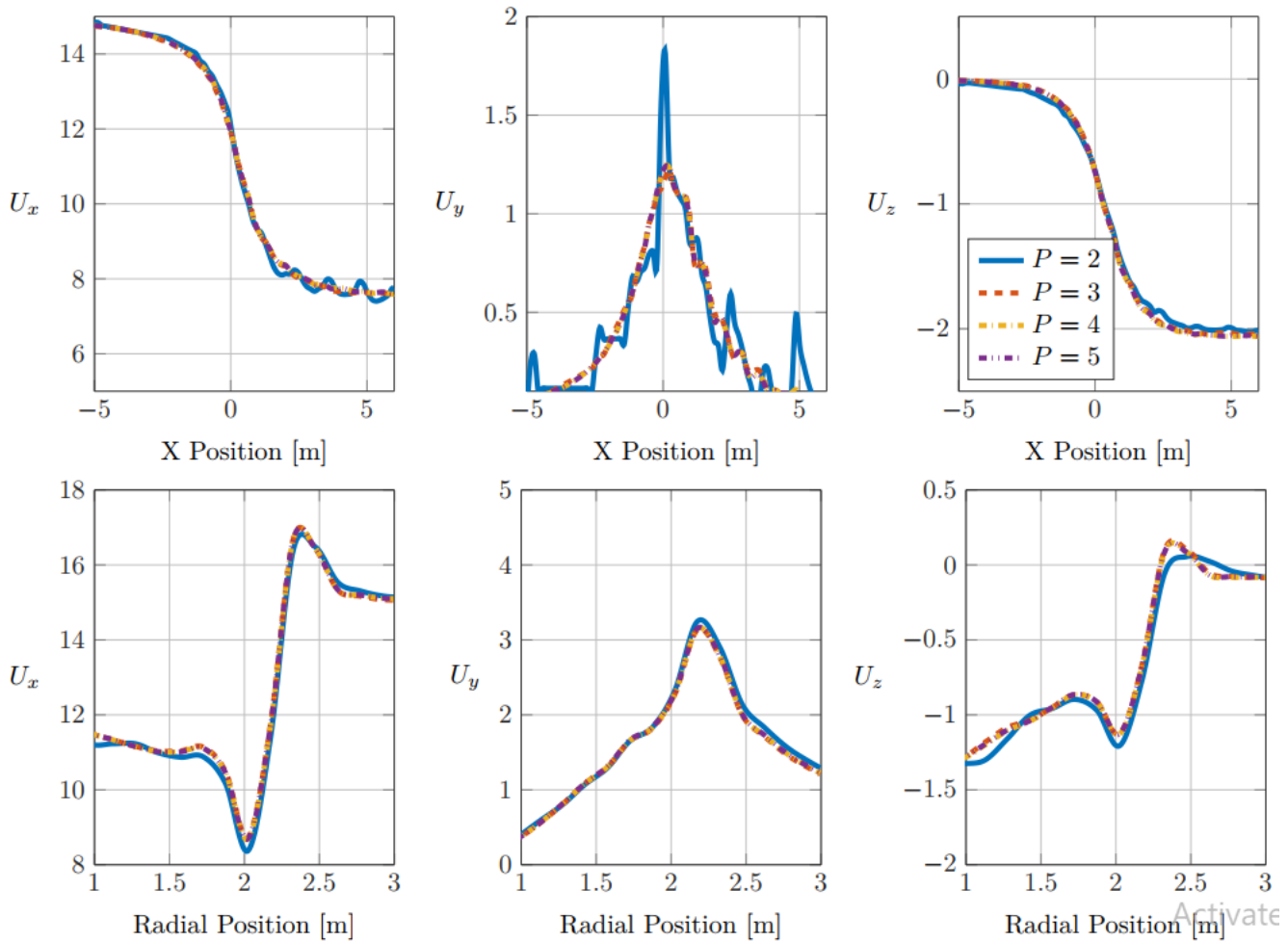
Figure 16: Axial (left), radial (centre), and tangential (right) wake velocities as a function of polynomial order. Top: Outer axial traverse. Bottom: Downstream radial traverse.
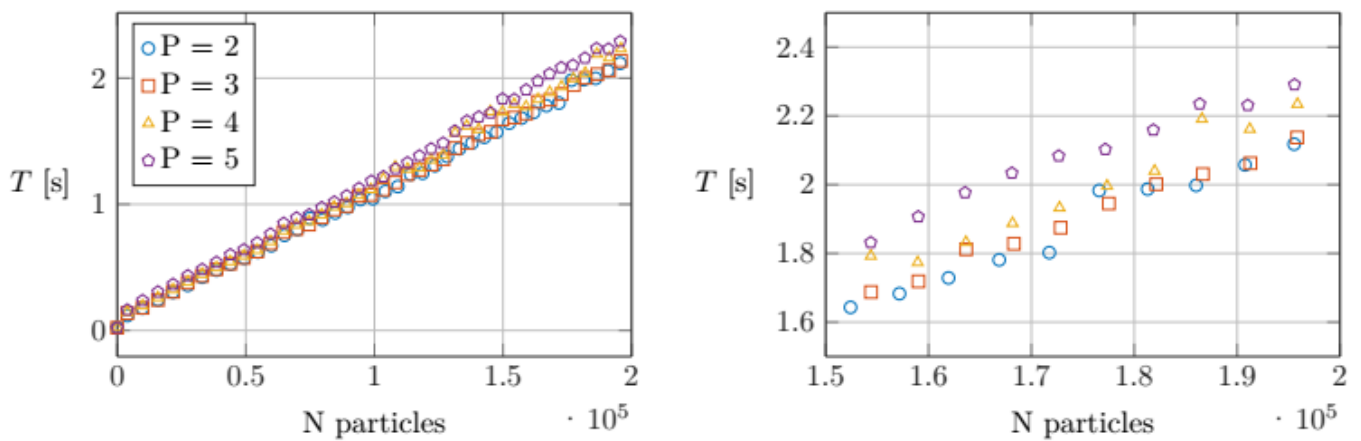

Figure 17: Computation time per simulation time step for different values of polynomial order P.

5.4.   INFLUENCE OF MAGNITUDE FILTERING FACTOR

The magnitude filtering is applied in order to ensure that the particle set size and dimension does not grow unbounded as a result of repeated application of the remeshing procedure. The influence of this has been investigated by simulating the turbine for a range of magnitude filtering factors F. The results of this investigation are shown in Figure 18. It is seen that the simulated physics of the wake are significantly altered for $F = 10^{-2}$. In this case a significant portion of the wake particle set is being removed and the integral influence on the wake velocities can be seen. For lower values of F, the differences between the solutions is much more difficult to discern. This confirms the heuristic argument made in Section 4.4.5 that as F decreases, the influence on dominant physical processes becomes smaller as the removed particles contribute less to the evolution of the particle set. It should be noted that the case $F = 10^{-1}$ was also simulated. For this case, the drastic removal of particles gave rise to highly unstable dynamics in the wake, along with strong fluctuations of the induced velocity on the blade.
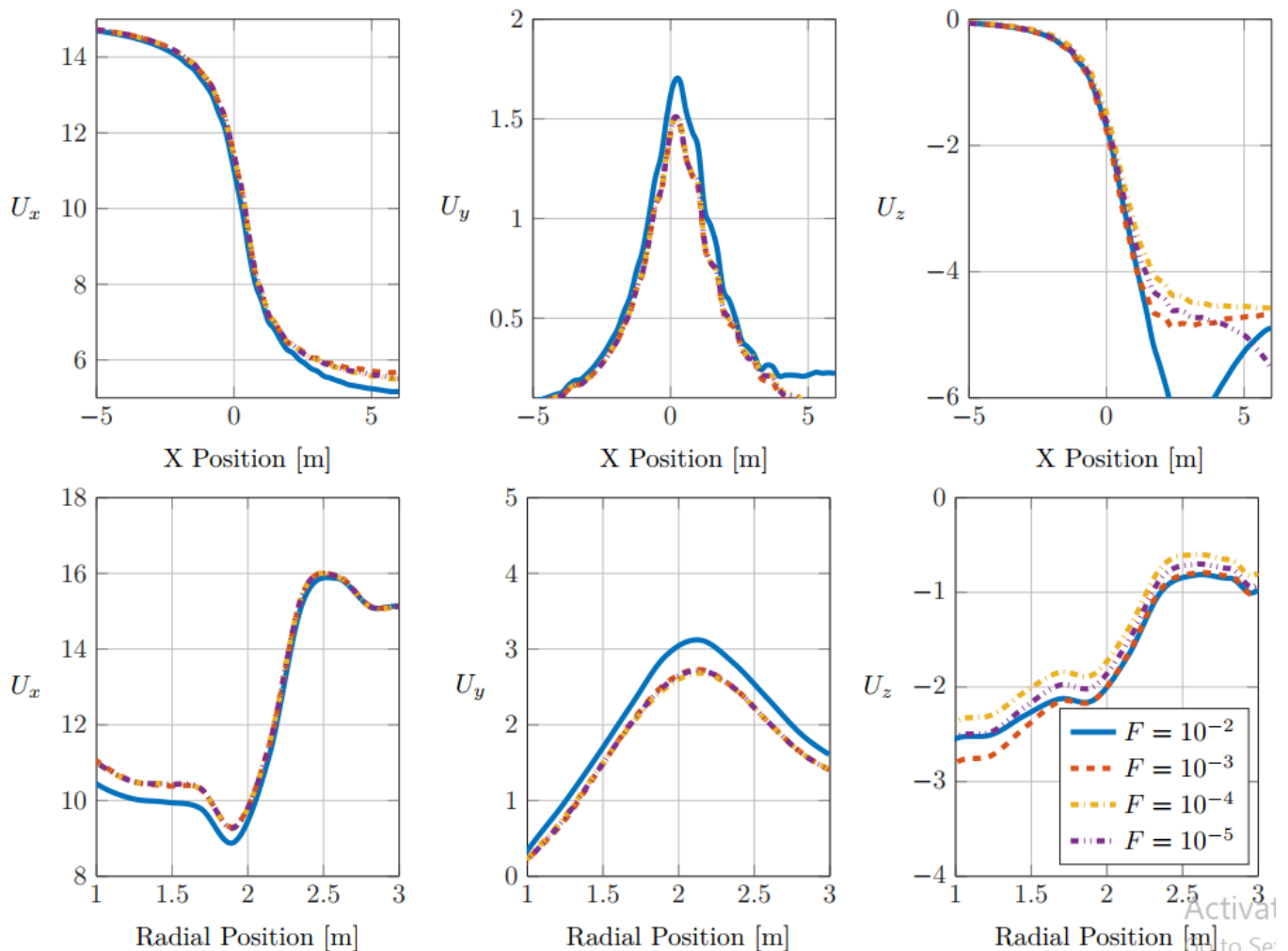

Figure 18: Axial (left), radial (centre), and tangential (right) wake velocities as a function of the magnitude filtering factor. Top: Outer axial traverse. Bottom: Downstream radial traverse.

The influence on integral turbine performance parameters is shown by inspecting the aerodynamic power of the turbine in Figure 19. Here the results demonstrate similar behavior. As F decreases, the solution is seen to converge. As described in Section 4.4.5, reducing F additionally has the effect that fewer active particles are removed from the particle set, thereby increasing the particle set and computation time. This is directly seen by monitoring the particle set size as shown in Figure 19. Here it can be seen that the particle set size essentially grows linearly with time. This is conceptually sensible, as the wake area is approximated well by a cylindrical section downstream of the turbine which constantly grows as the wake is convected downstream. It is demonstrated that the magnitude filtering factor is an effective measure to reduce total particle count and therewith simulation time.
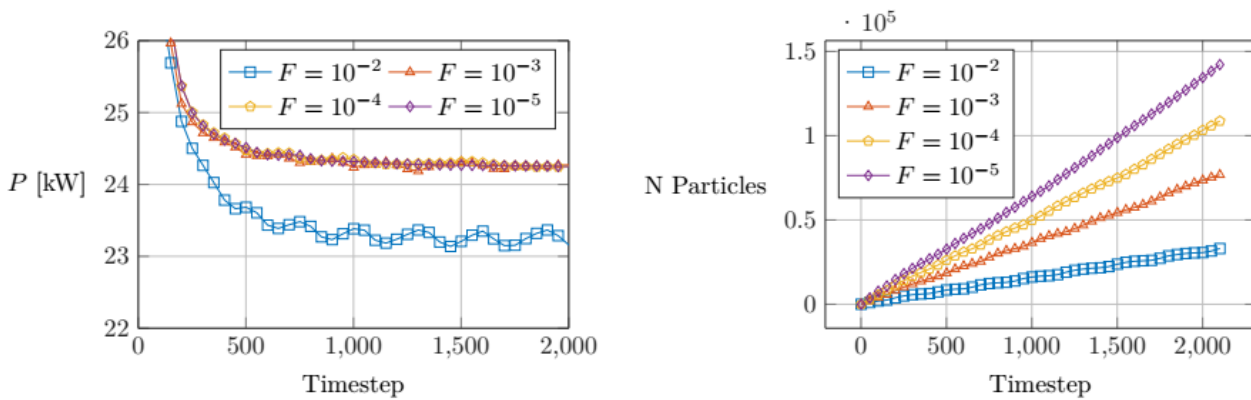

Figure 19: Left: Influence of the magnitude filtering factor on the aerodynamic power predicted in the simulation. Right: The increase in the size of the particle set is directly observed as the magnitude filtering factor increases.

5.5. INFLUENCE OF REMESHING PERIOD

Regularly remeshing the particle set is necessary to ensure that the particle source distribution is uniform and to avoid large concentrations of the Lagrangian mesh. It allows for the particles to be redistributed in such a way that vorticity moments are conserved. The process can very approximately be considered to be a kinematically consistent smoothing procedure of the vorticity field. The period N_R with which the remeshing is carried out (remeshing is carried out every N_R time steps) influences the compounded effect of this smoothing on the flow field. The remeshing procedure has a relatively low computational expense compared to the convolution step, such that this parameter can be chosen relatively freely without greatly impacting computational time. It was found that for the case that $N_R \geq 20$ the Lagrangian grid distortion became too large in the root vortex region, leading to diverging solutions. For this reason, the turbine has been simulated for the cases $N_R = 5$, 10 and 15 and the results are shown in Figure 20. For all following simulations, the grid size was set to $H_{grid} = D/40$.

It is observed that the results partially converge as the remeshing period is decreased. This is most strongly observed for the radial velocity U_y in the axial traverse and for the axial velocity U_x in the radial traverse. For other velocity components however, convergence is not observed. This shall be further discussed in the following sections, however in practice, for a remeshing period below 5, it becomes more practical to employ a quasi-Eulerian approach, where the particles are remapped to a regular grid at every timestep. This gives rise to advantages in some computational steps, and disadvantages in others and would

motivate a reformulation of the particle library. For this reason, the remeshing frequency $N_R = 5$ has been chosen, as this displays partially convergent behaviour and will be shown in the following sections to produce accurate results as compared to experimental values.
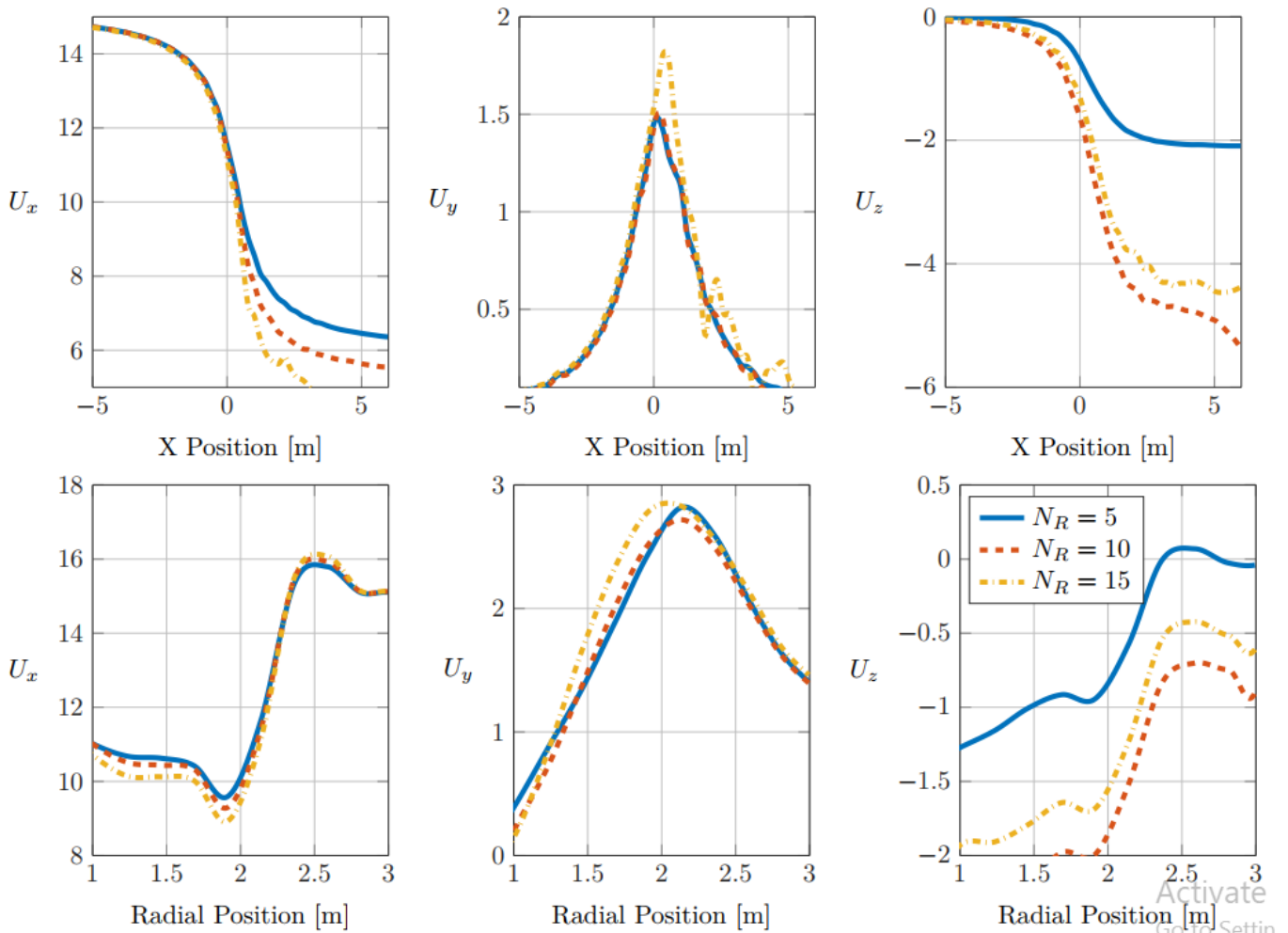

Figure 20: Axial (left), radial (centre), and tangential (right) wake velocities as a function of remeshing period. Top: Outer axial traverse. Bottom: Downstream radial traverse.

It is additionally observed that in Figure 21 that the converged aerodynamic power of the rotor is modified by the remeshing period, and converges with decreasing N_R. This is well explained by the smoothing effect caused by the remeshing scheme, which as described earlier acts as a relaxation scheme on the particle set. The entire particle set is remeshed, including those particles which are near to the blade elements. When this occurs, particularly for coarser grid meshes, this local redistribution causes a deviation of the induced velocities in the rotor plane. This is seen in Figure 21 for the three simulated cases. This effect is seen to amplify as N_R increases. This further motivates a low remeshing period, as induced velocity fluctuations at the blade have the potential to excite a structural response in aeroelastic simulations. This effect should be avoided as it may lead to undesired resonances of the turbine structure. This topic should be investigated in future works.
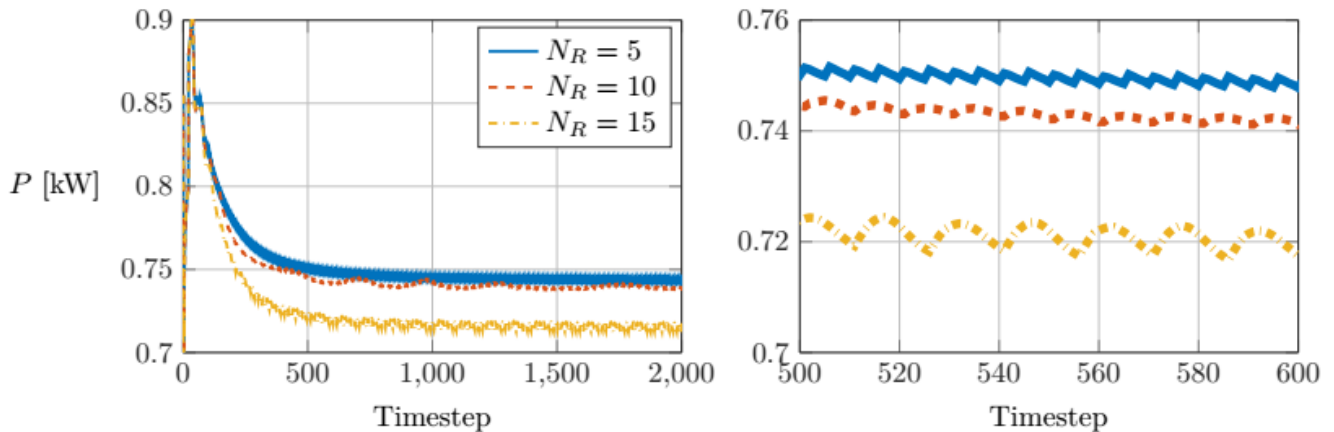
Figure 21: Discontinuities in aerodynamic power caused by the remeshing and the local redistribution of particles near the rotor. The shown values are purely qualitative and not representative of the actual yield of the turbine.

6.   VPML SOLVER VALIDATION

In order to demonstrate the efficacy of the VPML solver, numerous validation simulations have been carried out. The first validation cases shown in Section 6.1 are numerical comparisons of the VPML solver with other aerodynamic models for a steady, uniform inflow. The turbine geometry is taken from a well-documented reference wind turbine case, the IEA 10 MW [52].

In Section 6.2 the significantly more difficult case of comparing the wake velocities for an experimental turbine is investigated. Due to the extensive database of experimental measurements, the MEXICO rotor has been selected [56]. A comparison is made to both the experimental data set from the New Mexico experimental campaign and to numerical data from higher-fidelity solvers [54]. Wake velocity profiles are compared for both steady flow cases in Section 6.2.4 along with unsteady yawed cases in Section 6.2.5.

The experimental data for the New Mexico experiments were only captured for near-wake positions approximately one rotor diameter downstream of the rotor plane. This data therefore serves only to validate near-wake aerodynamics which are generally well captured with a vortex filament method. These comparisons therefore do not fully reflect on the strength of the VPML model over standard vortex filament approaches. The ability to treat higher order effects in the wake, which generally occur further than two rotor diameters downstream is facilitated by the particle method implemented in the VPML model.

6.1.   STEADY ROTOR LOADS

The first cases inspected are those of the steady loads acting on the blades of a reference wind turbine. The turbine has zero yaw and tilt angle, and is operating within a uniform inflow field. The blades and structure (drive shaft, tower, foundation) are treated as being rigid.

6.1.1. COMPARED SOLVERS

Two solvers have been compared with the VPML model.

UBEM: Within QB, the unsteady polar BEM model presented in Madsen et al. [44] has been implemented. This is applied here as this allows an improved aerodynamic treatment for both steady and unsteady aerodynamic cases as compared to a standard BEM model. For the simulations carried out here, the rotor plane has been discretized into 36 angular segments. A tip correction model has been used to ensure correct flow prediction in the tip region.

LLFVW: The LLFVW vortex-filament method within QB has been chosen to have a comparison with a second medium-fidelity wake solver. The blade element treatment is identical with that being used for the VPML method. As described in Section 5.1, the very near-field of the rotor is discretized with vortex filaments, implying that the flow is this region is expected to be comparable to that for the VPML model. For steady flow cases, the LLFVW model has been validated and the results are shown to agree well with BEM simulations [53]. Wake relaxation has been applied to remove initial transients from the solution and wake coarsening has been applied to reduce computational expense. By nature of the formulation of the LLFVW model, viscous effects and stretching are not treated within the model.

6.1.2. TURBINE DESCRIPTION

The turbine compared here is the IEA 10MW RWT [52]. This can be considered to be representative of modern offshore multi-MW wind turbines. The turbine is an upstream 3-bladed rotor architecture with a diameter of 198 m, a hub height of 119 m and a rated power of 10 MW. Although a structural model for this RWT is available, this has not been applied here to simplify the solver comparisons. The blade has been discretized with a cosine distribution to improve resolution at the blade tip and root with 50 blade elements. Turbine yaw, coning angle and shaft tilt are all set to zero in order to coincide with the assumptions of the BEM model. The airfoils are described by the FFA-W3 family of profiles. The polars have been calculated with the 2D CFD solver Ellipsys2D [54] assuming a fully turbulent boundary layer and do not utilize 3D corrections. This data was shared by the DTU wind energy group within the scope of a separate study [53].

The base grid size has been set as $H_{grid} = D/30$. Remeshing has been carried out every five time steps: $N_R = 5$. As described above, in order to align with the LLFVW, vortex stretching and viscous diffusion have been deactivated. The magnitude filtering factor has been set to $F = 5 \cdot 10^{-4}$.

6.1.3. RESULTS

The steady loads for three inflow velocities are shown in Figure 22. It is seen that in general the agreement between the three solvers is good. The tangential loads of the LLFVW appear to predict a greater induction near the blade tip, this may be explained by the Lagrangian treatment of the blade filaments, which ensure that the tip vortex filament remains approximately in the radial position it was shed from in the near field. With the VPML model the particles are regularly remeshed, which as described in Section 5.5 leads to a smoothing effect on the induction field. A similar effect is seen for the root region of the blade. The VPML

and LLFVW models agree perfectly in the root region for the case of an inflow velocity of 15 ms⁻¹. There is however discrepancy with the UBEM model, which may be attributed to stronger 3D interaction effects at the root of the blade not predicted by the UBEM model.
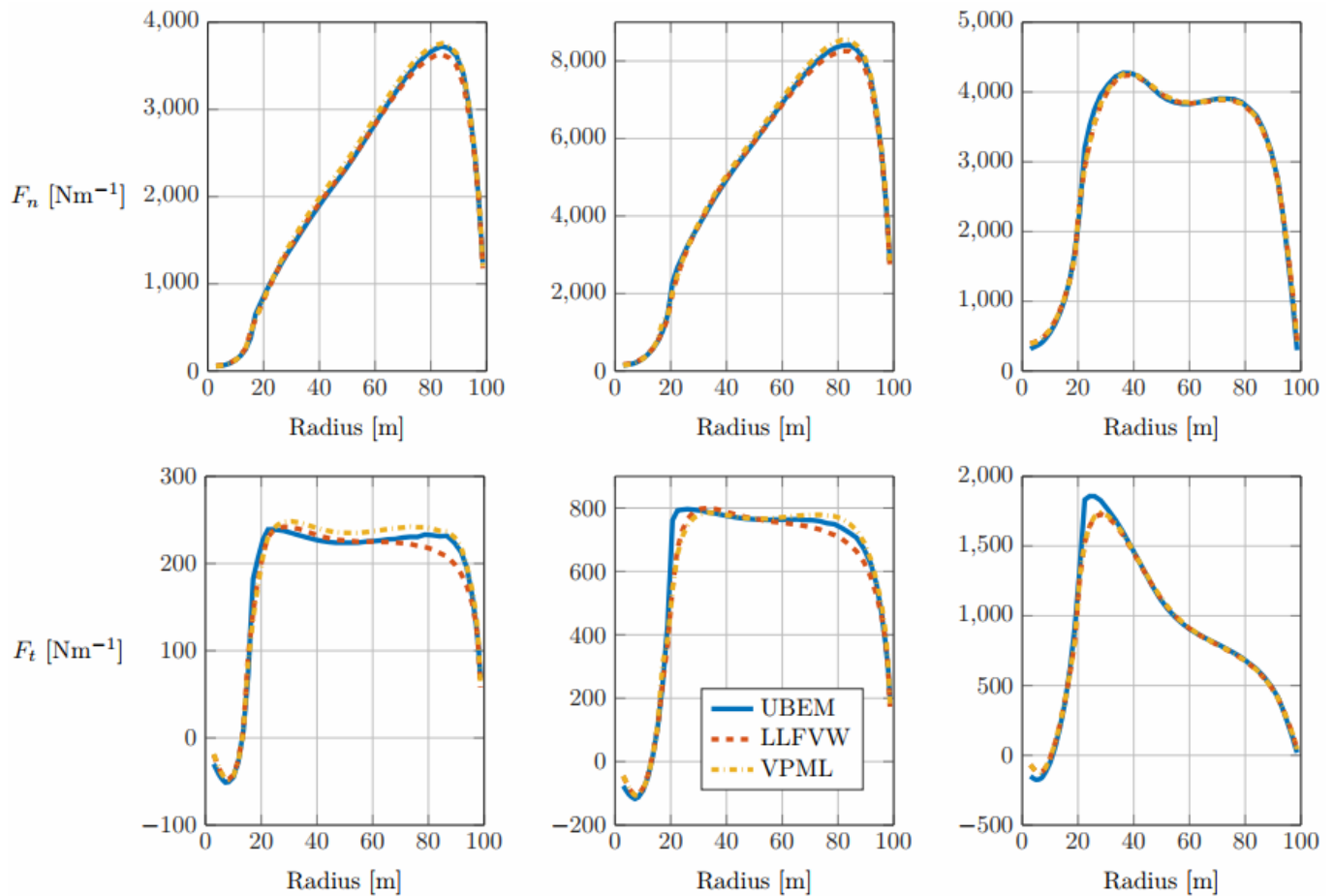

Figure 22: Steady normal (top) and tangential (bottom) blade loads for the IEA 10MW RWT. Free stream velocities left to right: 6, 10, & 15 ms⁻¹.

The good agreement between the solvers demonstrates that the induction in the rotor plane is well predicted by the VPML model. This provides a foundation to inspect the wake flow in the next section.

6.2.   WAKE VELOCITY COMPARISONS

In this section the accuracy of the VPML model for predicting flow quantities in the wake is assessed by comparing flow field quantities to the experimental data collected during the New Mexico wind tunnel experiments [55]. Comparison to numerous other flow solvers has been carried out. Error sources are discussed along with conclusions for practical application cases.

6.2.1. COMPARED SOLVERS

Three solvers have been compared with the VPML solver in this investigation. These are discussed here along with important simulation parameters. For all plots, the experimental values have been marked in the plot legends as **EXP**, the legend markers of the compared solvers are used for the following

descriptions. The UBEM solver has not been applied as this model provides no data about the variation of flow quantities in the wake.

LLFVW: The LLFVW vortex filament method previously existing in QB has been applied for comparison with a second medium-fidelity wake solver. The blade element treatment is identical with that being used for the VPML method.

FLOWer: The FLOWer CFD solver developed at the Institute of Aerodynamics and Gas Dynamics (IAG) at the University of Stuttgart [58] is a block-structure FV solver. This employs an unsteady RANS approach with the one equation Spalart-Allmaras model (for the unsteady cases and 24 ms^{-1} case) and the two-equation $k - \omega$ SST model for all other cases. The meshing of the blades uses a C-O topology for the axial cases and a C-H topology for the yawed cases generated with the tool Automesh. The number of cells varies between 10-20 million depending on the application case. An overset grid technique has been applied, which has an adaptive mesh for the wake region.

OpenFOAM: The Fraunhofer Institute for Wind Energy simulated the New Mexico using the open-source OpenFOAM FV solver. A delayed detached eddy simulation (DDES) model was applied which makes use of the Spalart-Allmaras turbulence model in the vicinity of the walls and an LES approach far away from walls. The mesh is identical to that used for the IAG solver.

These were chosen so as to provide a range of solver fidelities for comparison. The latter two models are fully developed CFD solvers and are expected to deliver the most accurate results (see Section 2.2). The LLFVW model is a medium-order method which is more comparable to the VPML developed in the work here. It is interesting to note that in the MexNext Phase III analysis, the lifting line codes have not been applied to model the wake induction in the wake analysis sections. This follows from the discussion in Section 2.2.2, where it is described that this style of modelling is more applicable in the very near wake, where an inviscid flow well approximates the flow regime.

6.2.2. TURBINE DESCRIPTION

The simulations in this analysis have been carried out with a numerical twin of the MEXICO rotor (**M**odel Rotor **Ex**periments **i**n Controlled **Co**nditions) [56], visualised in Figure 23. The experimental data was recorded in the New Mexico wind tunnel experiment in 2014 [57] and analysed in IEA Wind Task 29 (MexNext-Phase III) [54]. This dataset was chosen due to the comparatively complete turbine geometric definition, allowing accurate reproduction within QB. In addition to this, a significant amount of experimental data from MexNext Phase III is available including blade and rotor forces, on-blade pressure measurements and velocity measurements in the wake along axial, radial and azimuthal traverses. These data sets allow for a quantitative comparison with the wake behavior predicted by the VPML wake solver.
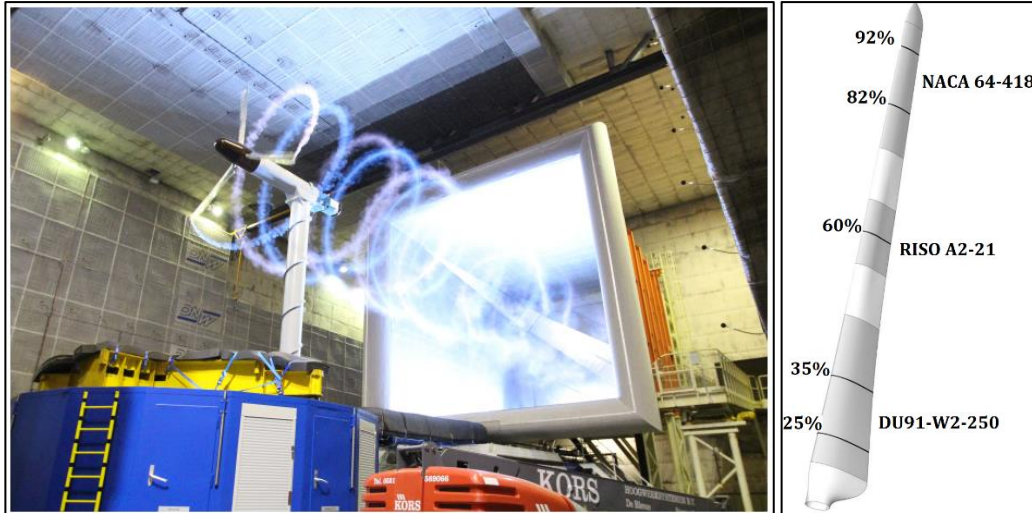
Figure 23: MEXICO rotor during operation- image from [57] (left). MEXICO Blade geometry- image from [1].

The turbine is an upstream 3-bladed rotor with a tip and root diameter of 4.5m and 0.25m, respectively. The blade has been designed for an optimal TSR of 6.7 and is composed aerodynamically of three airfoils sections: The DU91-W2-250 in the root region, the RISO A2-21 in the mid-span region and the NACA 64-418 in the tip region, connected by morphing sections. The relative positions of these are illustrated in Figure 23. The turbine was operated in an open test section in order to reduce blockage effects which may act on the wake. The rotor was operated with a constant rotational rate of 425.1 RPM and the tunnel operated at three flow velocities: 10, 15 and 24 ms^{-1}. With these velocities, the operational TSR values of turbine were 10, 6.7 and 4.16, respectively. Flow velocities upstream and downstream of the rotor plane were recorded using particle image velocimetry (PIV). Three probe traverses were applied in the experiments, these are summarised in Table 2. It should be noted that a right-handed coordinate system has been applied with its origin at the rotor hub, positive x pointing downstream and positive z pointing vertically upwards.

Traverse	X coordinate [m]	Y Coordinate [m]	Z Coordinate [m]
Inner Axial	$-5 \leq x \leq 6$	0.5	0
Outer Axial	$-5 \leq x \leq 6$	1.5	0
Upstream Radial	-0.3	$0 \leq y \leq 3$	0
Downstream Radial	0.3	$0 \leq y \leq 3$	0

Table 2: PIV Traverses of the New Mexico campaign.

For the comparisons in this report, the outer axial and radial traverses have been analysed and is highlighted in the above table. The inner radial traverse presents two issues. Firstly, the datasets with regards to the inner radial PIV traverse are much less complete than the corresponding outer traverse.

Secondly, the effect of the nacelle and hub region are still quite dominant in this region and this is modelled with neither the VPML nor the LLFVW models. For this reason, the inner traverse has been omitted from the analysis. Similarly, the upstream radial traverse has been omitted as the region of interest for the solver is the wake of the turbine. In addition to the aforementioned traverse, azimuthal PIV traverses were also conducted. As they have been deemed to contribute little new findings to the analysis, they also have been omitted.

6.2.3. TURBINE DEFINITION WITHIN QBLADE OCEAN

The turbine definition includes a complete geometric description of the MEXICO rotor blade. The provided chord and twist distributions have been applied in order to define the sectional geometric properties within QB using the corresponding blade definition module, as shown in Figure 24. It would have been possible to generate the airfoil polars with XFoil using the airfoil tool within QB and then extrapolate them using the 360° polar module. However, it was decided to apply the supplied airfoil polars for the NextMex Phase III comparison investigations. In preliminary testing it became quickly obvious that the provided polars led inevitably to inconsistent circulation distributions, particularly in post-stall conditions (TSR 4 case). It has been concluded that this is the result of two contributing factors. Firstly, a single airfoil polar is specified for each airfoil for all three cases, despite the fact that there is a significant variation in Reynolds number at the three operational states. Secondly, the discontinuous nature of the 360° polar extrapolations carried out can be seen in the data, particularly for the DU91-W2-250 airfoil.

These factors were found to greatly influence the behaviour of the circulation distribution on the blade. This directly affects the vorticity distribution shed into the wake and the resulting induction distribution. These points will be further elaborated upon in the discussion of the results. The 360° extrapolation of the DU91-W2-250 airfoil was subsequently repeated within the corresponding QB module in an attempt to generate more consistent results, this is similar to the work carried out by the CENER group [55]. At transition sections (see Figure 23), interpolated airfoil polars between the corresponding sections have been used to ensure continuity. In order to avoid aerodynamic discontinuities at the blade tip and root, a linear interpolation of the blade chord and twist distribution has been carried out such as to mimic the actual blade geometry. The root section is defined by a cylindrical section. The airfoil sections have all been shifted such that their aerodynamic centers lie precisely on the blade axis (Y) as seen in Figure 24.
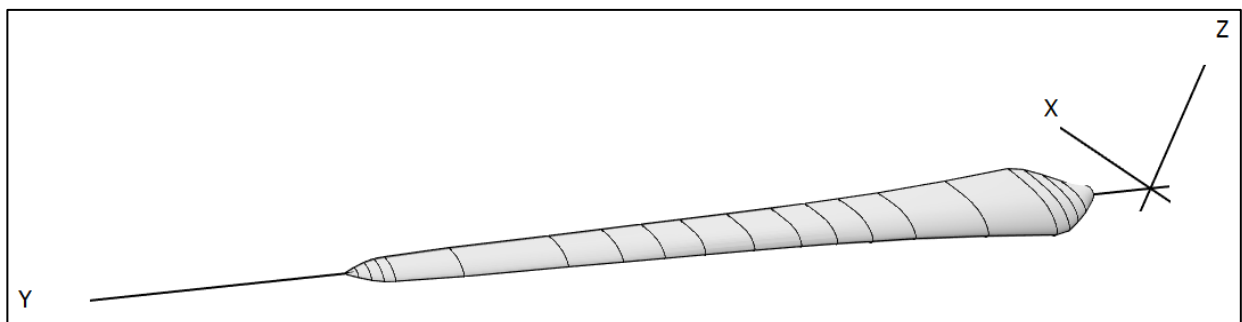

Figure 24: MEXICO Blade definition within QB.

6.2.4. STEADY FLOW CASES

In this section the test cases carried out in round 1 (WP2) of the New Mexico campaign have been simulated and the results are compared to the solvers described in Section 6.2.1. As the turbine was not yawed in these tests, the turbine and wake (under consideration of an appropriate corotating coordinate system) can be considered as a steady flow case. The tests were carried out for three values of the free stream inflow velocity corresponding to the experimental measurements. PIV data was collected in the wake of the turbine, allowing comparison to the output of the VPML solver.

The outer axial traverse is now inspected for the operating states investigated in order to demonstrate the ability of the VPML model to predict wake velocities. A few important points should be made here. The axial velocity traverse is taken approximately 1D upstream and downstream of the rotor plane, and as such this validation is only representative of the near-wake of the rotor and more detailed information regarding turbulent statistics and shear stresses would be required for validation of the far wake flow with the VPML solver. The experimental data has been collected in rectangular PIV planes which do not overlap at all positions, explaining the apparent gaps which appear.
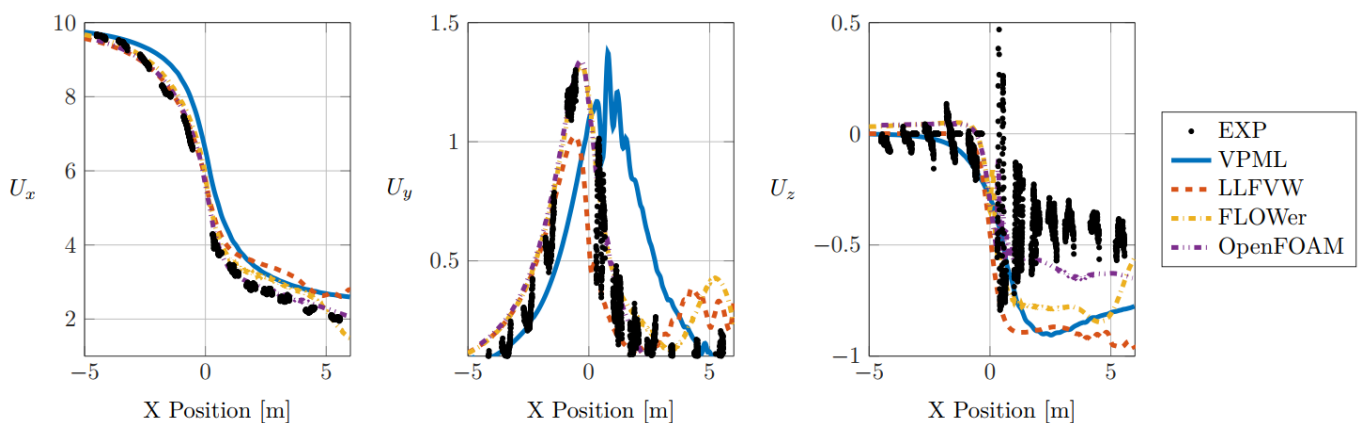

Figure 25: Velocity components along an axial traverse of the MEXICO rotor for a free stream velocity of 10 ms^{-1} (TSR 10).

The wake for an inflow velocity of 10 ms^{-1} is shown in Figure 25. It is seen that the CFD solvers both match quite well with the experimental results. The axial velocity predicted by the VPML and LLFVW models is slightly higher than that of the CFD solvers. Testing demonstrated that this effect was alleviated by deactivating the stretching in the particle strength evolution. This suggests that this error is associated with excessive field relaxation within the particle solver and may be better understood with a more in-depth analysis of the conservation of particle set integrated properties. This is outside of the scope of this work, however this point will be discussed again for the next OP. It is observed that the LLFVW model predicts a slight deviation in the axial velocity downstream of the rotor. It was observed in the analysis that this may be an indication that the root vortex accumulation is not being treated correctly and was observed also in the VPML results for the case when stretching was deactivated. This phenomenon was only observed for the high blockage case (TSR 10). In the rotor plane the CFD solvers both agree very well with the radial velocity component. The VPML model appears to demonstrate a displacement of the velocity curve. This is very likely coupled directly with the reduced induction predicted by the VPML

model. This represents the wake expansion caused by streamtube blockage and is therefore an indicator for accurate mass conservation of the solvers. Interestingly, both CFD solvers predict that a second peak in the radial velocity occurs, which disagrees with the experimentally recorded values. All solvers over-predict the tangential velocities in the wake and fail to predict an oscillation, likely caused by the tip vortex. This quantity represents wake rotation caused by the rotor.

The wake velocity profiles for the design TSR of 6.7 are shown in Figure 26. Here agreement with the experiment is seen to improve for all models. The axial velocity profile of the axial traverse matches well with experiments. The radial velocity predictions demonstrate that the expansion predictions of the VPML model are lower than those of the other solvers upstream of the rotor and in the rotor plane. Continuing the discussion of the previous paragraph, in the axial velocity plot of Figure 26, an additional dotted line is shown. This is the velocity prediction of the model with vortex stretching deactivated, the solid line (in that plot) indicates the axial velocity prediction of the VPML model with vortex stretching activated. This is again a possible indication of underrelaxation caused by the stretching terms. It is described in [51] that the stretching term is dominated by the near field. It may therefore be the case that the grid size must be reduced in order to correctly capture stretching effects in the field, however tests carried out with a finer grid tended to negate this hypothesis. Further testing is required to determine the causal factor leading to this. The behaviour of the radial velocity term matches the experiment well although the maximum peak is not reached. The behaviour of the tangential velocity is approximately captured as well. However, the strong fluctuations caused by vortex passing do not appear to be predicted well by any of the solvers.
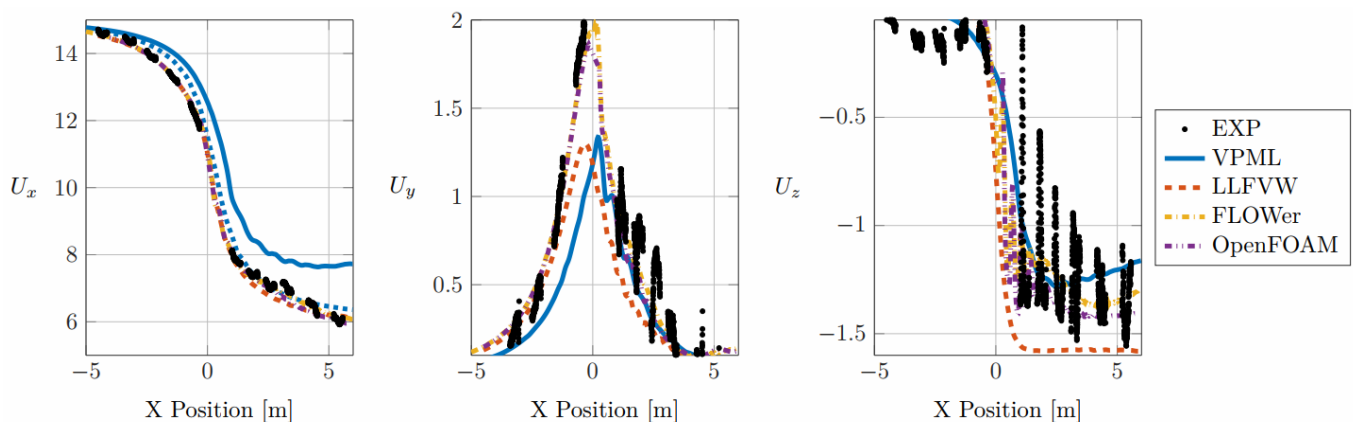

Figure 26: Velocity components along an axial traverse of the MEXICO rotor for a free stream velocity of 15 ms^{-1} (TSR 6.7). The dotted line for the axial velocity plot indicates the solution with vorticity stretching deactivated.

The induced velocities in the wake for the low TSR case are shown in Figure 27. For this OP wake induction is generally lower than for the other OPs, as the rotor is operating with a lower power coefficient. In this case, the induced velocities along the axial traverse are under-predicted by both the VPML and LLFVW models. This trend is reflected for both the radial and tangential velocities, where strong fluctuations are observed in the experimental conditions, and captured only by the OpenFOAM CFD model. The fluctuations can be explained by the passing of the tip vortices. As opposed to the previous tests, here the tip vortices remain discrete and coherent (not merging simply into a shear layer) relatively far behind the rotor. The trends appear to be similar to the previous OPs but are somewhat amplified for this case.
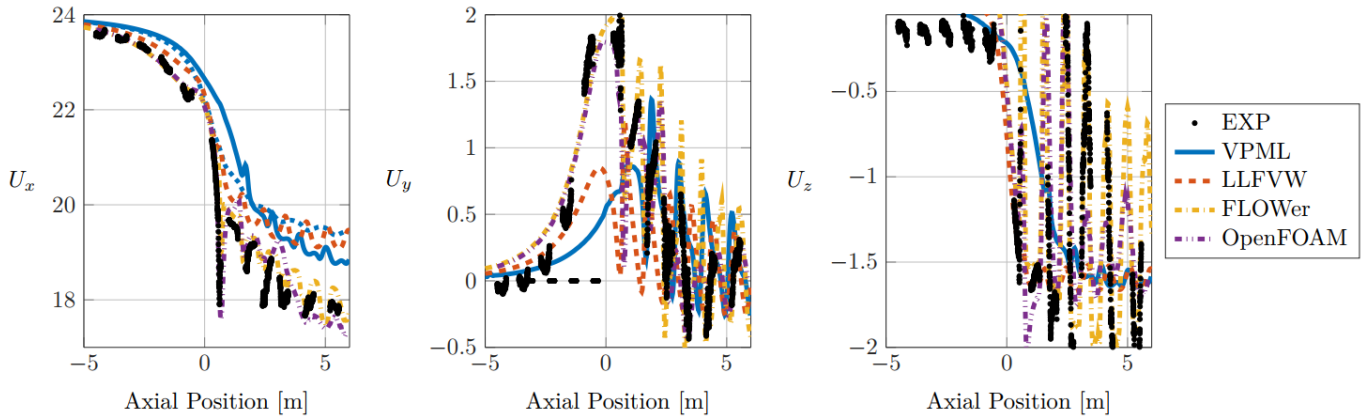
Figure 27: Velocity components along an axial traverse of the MEXICO rotor for a free stream velocity of 24 ms⁻¹ (TSR 4.1). The dotted line for the axial velocity plot indicates the solution with vorticity stretching deactivated.

Although it is observed that there are quantitative disparities, in general the qualitative behaviour of the solvers appears to match well with the experiments. As discussed in the introduction, it is believed that these are connected strongly with specification of lift and drag polars and that accurate specification of these may remedy many issues in the predictions. In addition to this, a detailed investigation on the influence of both the introduction of the stretching term along with the shear stress terms is required for a fully qualitative analysis of the flow cases described here. These are outside of the scope of this document, which aims simply to provide a preliminary exhibition of the capabilities of the VPML model.

6.2.5. UNSTEADY FLOW CASES

In order to demonstrate that the VPML model is capable of simulating unsteady wake evolution, the yawed experiments carried out in round 2 (WP3) of the New Mexico experiments have been simulated. The results are again compared to the solvers described in Section 6.2.1. In the experimental tests, the turbine was operated at the same inflow velocities of the steady cases described in Section 6.2.2 with additionally a yaw angle of 30°. The effect of the yaw angle on the rotor is to change the relative velocity vector of the inflow field relative to the blade section during rotation. The angle of attack of each blade section is then constantly changing, along with the sectional blade loads. This influences directly the vorticity shed into the wake and therewith the velocity profiles in the wake.

The non-stationary flow on the blade sections induced by the changing angle of attack can give rise to a phenomenon known as dynamic stall [43], where the lift and drag coefficients deviate significantly from the static values. The magnitude of these deviations is a function of the magnitude and rate of change of the angle of attack. To account for the dynamic stall, the Øye model has been applied in QB. In this model, the dynamic stall is treated as a time-lag effect of separation [59]. The dynamic lift and drag coefficients are calculated as:

$$C_{l,dyn} = fC_{l,att} + (1-f)C_{l,sep} \tag{13}$$

$$C_{d,dyn} = C_{d,st} + 0.5\left(C_{d,st} - C_{d0,st}\right)\left(\sqrt{f_{st}} - \sqrt{f}\right) - 2.5(f - f_{st}), \tag{14}$$

where the subscripts att, sep and st refers to values at attached inviscid, fully separated viscous and static conditions respectively. The variable f depends upon a time lag parameter, set in the work here to be 8 as this is generally considered to be a suitable choice for this parameter. For a detailed discussion of this implementation, the reader is referred to Bergami & Gaunaa [60].

As with the previous section, the velocities downstream of the rotor have been inspected. For brevity, only the downstream radial traverse is inspected. For the shown datasets, as specified for the MexNext Phase III comparisons, the induction values have been averaged over a rotor rotation. The case of a freestream velocity of 24 ms^{-1} has been omitted from the comparison as a significant portion of the experimental data was not captured in the experimental datasets. Furthermore, only the case of a freestream velocity of 10 ms^{-1} has been shown as this presents the most challenging case and the 15 ms^{-1} case showed fundamentally similar results.

The induced velocities for an inflow velocity of 10 ms^{-1} are shown in Figure 28. Numerous important observation can be made here. The LLFVW wake method appears to predict well the velocity in the near-rotor plane, motivating the use of a combined filament and particle method for the near field aerodynamics as described in Section 5.1. In addition, the asymmetry of the wake is shown to be predicted well by all models for all velocity components. However, a slight lateral shifting is observed for the VPML model when the axial velocity is considered. This was found to be influenced by the choice of stretching method on the evolution of the particle field. A detailed discussion is beyond the scope of the demonstrations here. The agreement of the y and z-velocity components is found to be much better for both the VPML model as well as the LLFVW models. Inspecting the positions of the velocity peaks, which effectively represent the location of the tip vortices, it can be seen that all models predict a wake deflection in the same direction. This illustrates that the VPML model is applicable to the simulation of wake steering for application to farm control problems.
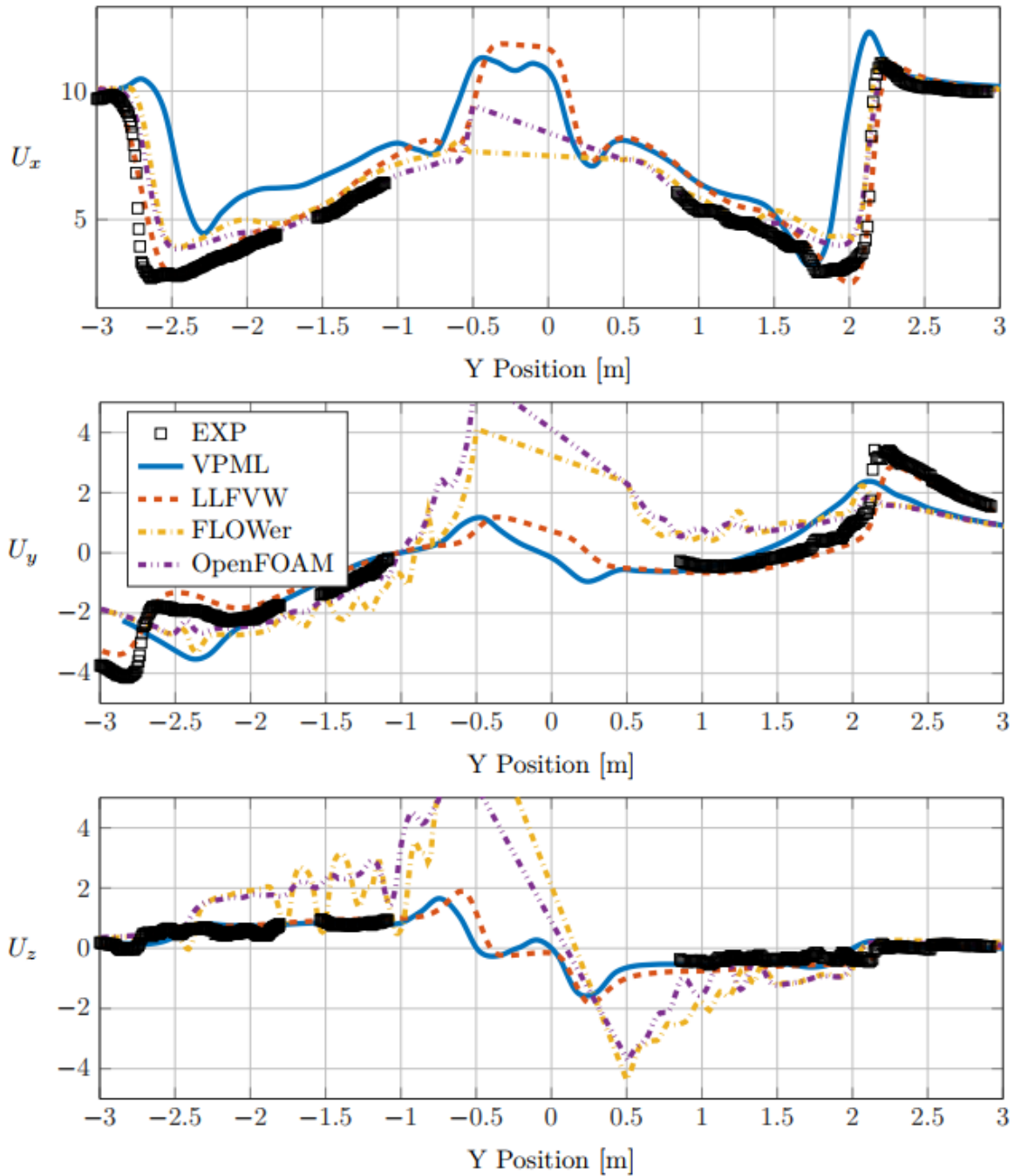
Figure 28: Radial velocity traverses in a plane parallel to the yawed turbine for an inflow velocity of 10 ms^{-1}.

6.3.   SUMMARY

A number of simulations have been carried out to demonstrate the efficacy of the VPML hybrid Eulerian-Lagrangian flow model. In Section 6.1 the VPML model was applied to the IEA 10MW RWT and the results of the steady blade rotor and tangential loads were compared to a low-order BEM method and a comparable medium-order LLFVW method based on a vortex filament treatment. In this case all three rotors made use of the same aerodynamic polars. This implies that any discrepancies which may arise are not a function of the blade element treatment, but rather the wake model. The qualitative and quantitative agreement between all three solvers was excellent, indicating that the calculation of the

induction in the rotor plane is well captured by the VPML model. This supports the conclusion that for steady cases the VPML method functions well as all three models, markedly different in their formulations, agree.

In Section 6.2 the MEXICO experimental rotor was investigated. It was found during preliminary investigations that the specification of the polars gave rise to discrepancies in the blade loading as compared to experimental results. As the VPML model relies heavily on the specification of accurate airfoil polars, this was found to have an influence on the predicted induction of the wake. In Section 6.2.4 the wake velocities in axial, radial and tangential directions were compared to experimental values, to the output of the aforementioned LLFVW model and to two high-fidelity CFD solvers. It was observed that the reduced induction in the rotor plane affected the velocities in the wake. Nevertheless, good general qualitative agreement was found with the other models. In Section 6.2.5 the much more challenging case of a yawed turbine was investigated. The numerical results of the VPML solver agreed qualitatively well with the experimental values. However, it was observed that the polar specification gave rise to uncertainties in the wake velocities predicted by the model.

7. APPLICATION OF THE VPML MODEL TO UNSTEADY FLOW CASES

One of the main application cases for the VPML model is the simulation of unsteady far-wake cases. As an illustration of the capability of the new solver, a number of exemplary cases have been simulated. A full-scale numerical turbine has been simulated in order to demonstrate the applicability of the method to full-scale turbine geometries. It should be noted that the simulations are not performed for the purpose of validation, but rather to demonstrate the applicability and stability of the VPML solver.

7.1. TURBINE DESCRIPTION

For the application cases, the DTU 10MW RWT has been chosen. The turbine has a hub height of 119 m, and a rotor diameter of 178.3 m. The blade definition and airfoil polars have been taken directly from the definition document [8]. Unlike the cases considered for the validation simulations, the DTU 10MW RWT was simulated aeroelastically. The structural dynamics are simulated with the CHRONO multiphysics library available in QB. This choice represents a realistic geometry for a multi-MW turbine and the numerical stability of the VPML solver can be demonstrated for turbine simulations where large aeroelastic deflections occur. The optimal parameters for the wake simulation have been taken directly from Section 5, with the exception of the grid size. This has been to the value $H_{grid} = D/60$ in order to allow visualisations of discrete vortex filaments in the wake.

7.2. YAWED TURBINE

The first unsteady case considered is that of a yawed turbine. The DTU 10 MW RWT [8] has been simulated with a rotation rate of 8.564 RPM, in a uniform inflow of 10 ms^{-1} (TSR=8) and a constant yaw angle of 30°. The turbine has been simulated with a time step corresponding to an azimuthal discretisation of 3°. Such a large yaw error is very unlikely to occur in practical scenarios. Nonetheless, this was chosen to emphasise the capture of important physical features. Two visualisations of the wake deflection are shown in Figure 29. It can be seen how the asymmetrical distribution of vorticity in the rotor plane gives rise to a deflection

of the wake. This feature has been suggested as a method to reduce wake interaction between turbines in a wind farm [62]. No additional model parameters were required for simulation of this case within the VPML solver. The vorticity formulation of the solver allows for such phenomena to be naturally captured by the method. This modelling approach simplifies greatly the wake treatment, as correctional models are not necessary and the solver framework can proceed without parameter tuning. In addition to this, adaptive meshing is used to ensure that only regions of interest are discretised for the calculation of the solution.
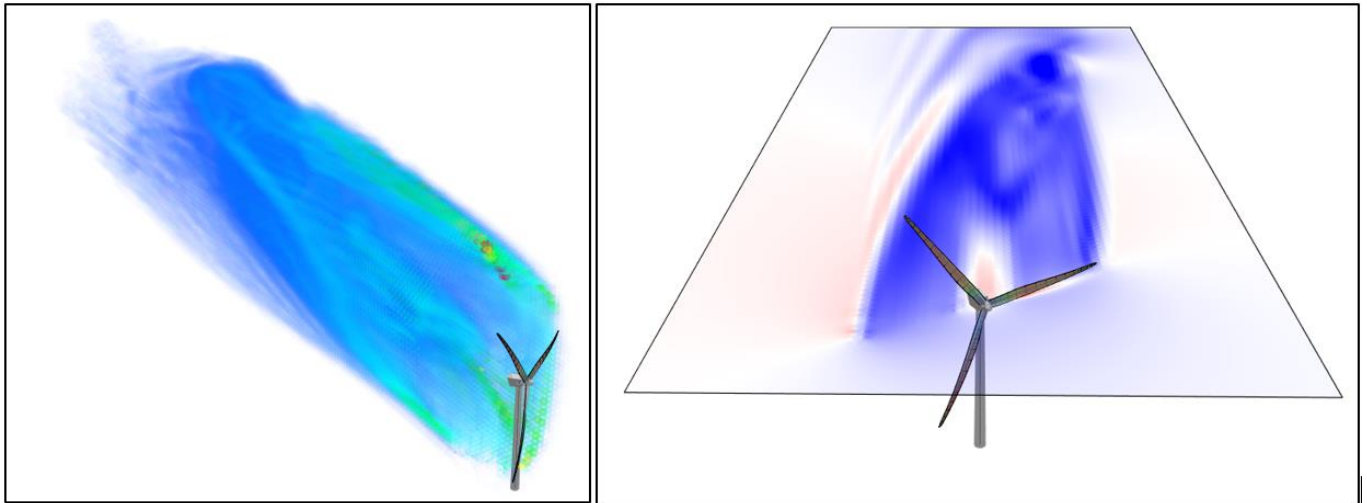

Figure 29. Yawing turbine. Left: Wake vorticity volume rendering. Right: Axial velocity cut plane downstream of the rotor. The wake deflection is observed to be a natural consequence of the vorticity dynamics captured within the VPML model.

7.3.   PITCHING TURBINE

The second considered case is that of an offshore floating turbine which is undergoing a pitching motion. This is a scenario which is likely to occur when the turbine is exposed to a frontal gust and the blade pitch response of the controller is not quick enough to counter the increased aerodynamic thrust. The turbine will pitch back under the action of the increased thrust and oscillate back and forth until an equilibrium position is again reached. This has direct application to the methodologies investigated in WP3 and WP4 of the FLOATECH project.

This case presents a modelling challenge in that the turbine rotates through its own wake during the pitching motion. This gives rise to very strong shear fields in the vicinity of the blades. Simulating such an event with a vortex filament method invariably gives rises to numerical issues as the filaments are not well suited to the resolution of such shear gradients or their spatial deformation [63]. This problem is not encountered when resolving the field with particles due to their improved connectivity properties.

 In order to simulate this case, a harmonic motion of the floating turbine in pitching direction was applied with an amplitude of 15° and a frequency half that of the rotation rate of the rotor. The situation is again highly unrealistic and was chosen in order to amplify the physical phenomena present in such a scenario. A visualization of the velocity field is given in Figure 30. Two observations can be made regarding the

vorticity field in the wake. The first is the very strong vorticity distribution generated by the motion of the turbine in the rotor plane. The second is the strong deformation of the vorticity filaments in the wake. The interaction and merging is a result of the vortex stretching and viscous diffusion of the vorticity field, both phenomena which are not well captured by a filament method.
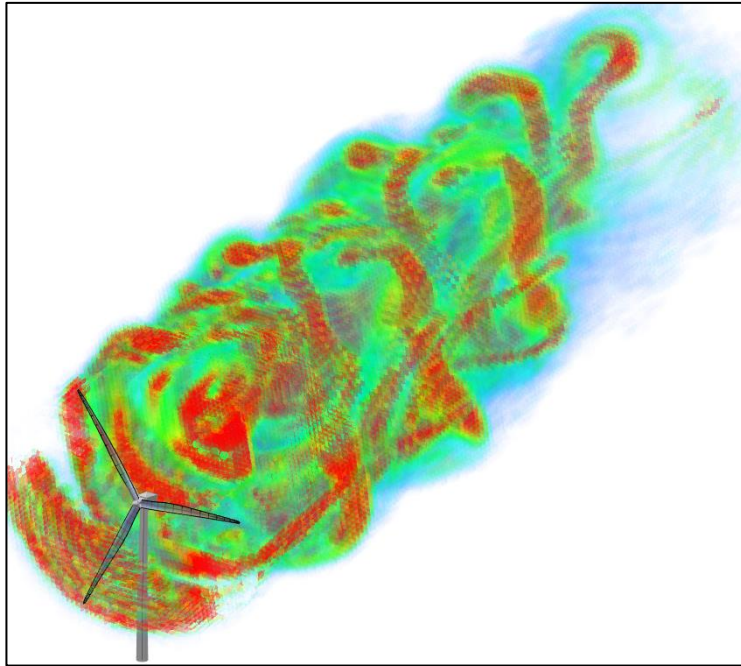

Figure 30: Unsteady wake resulting from the harmonic pitching motion of an offshore turbine. The vorticity scaling is based upon the magnitude of vorticity.

Two velocity cut planes are shown in Figure 31. These demonstrate the x and y-velocity components in the wake. A few interesting points can be observed. The irregular spacing of the tip vortices which arises due to the pitching motion is clearly seen in the x-velocity plot. In addition to this, the strong deformation of the wake centreline can be observed in the y-velocity plot.
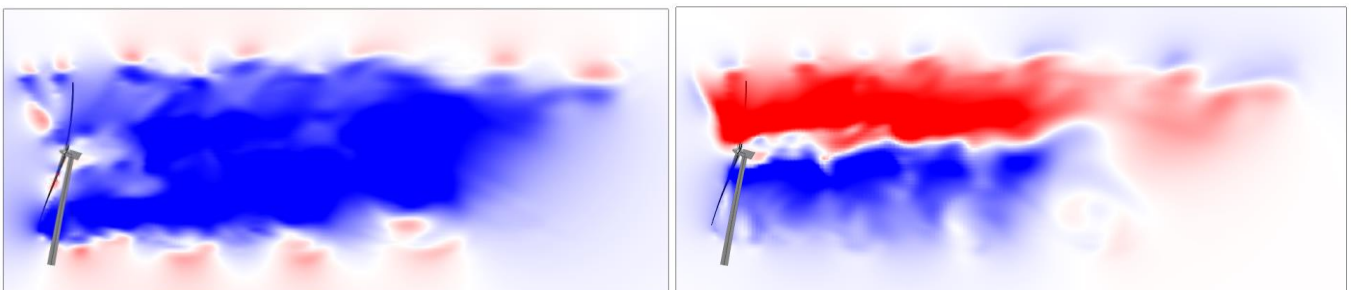

Figure 31: Velocity cut planes in the wake of a pitching offshore turbine. Color scale based on x (left) and y (right) velocity fields.

8.   CONCLUSIONS AND OUTLOOK

In this report a new aerodynamic model, aimed at treating higher order aerodynamic effects in the wake of a wind turbine, has been presented. The Vortex Particle Multilevel (VPML) solver has been developed based on the concept of vorticity transport and the vortex particle method. This style of solver allows for the treatment of higher order physical effects, often neglected in lower order models, such as the influence of vortex stretching and viscous effects on the evolution of the wake. The VPML model is well suited to the modelling of far-wake aerodynamics, particularly in cases where the turbine is undergoing unsteady motion, such as on an offshore floating platform. The solver will be applied in the FLOATECH project to the simulation of floating offshore wind turbines for the investigation of feed-forward wave-based control strategies in WP3 and to the active wake mixing concept of WP4.

An overview of the state-of-the-art of aerodynamic models used in the simulation of a wind turbine and its wake were described in Section 2. Here the motivation for the implementation of an accelerated medium-order solver based on the vortex particle method was described. In Section 3 the existing aerodynamic models currently in QBlade Ocean were described.

In Section 4 the fundamental theory underlying the vortex particle method was described. Directly evaluating the vortex particle method has a computation complexity which scales with the square of the number of particles. This expense must be reduced in order to allow for accelerated simulation of the flow field. The method chosen to accelerate the calculation was the Multilevel Multi-Integration Cluster (MLMIC). This was applied to the vortex particle method in the VPML solver. The calculation procedure of the MLMIC and the extraction of the corresponding field quantities with the VPML was described along with important numerical procedures relative to the suitable functioning of the vortex particle method.

The sensitivity of the VPML solver to important solver parameters was carried out in Section 5. The dominant simulation parameters, a description of their influence and a refinement study were carried out for each parameter in order to provide a general overview for suitable parameter choice to ensure accurate simulation results.

A validation of the VPML model was carried out in Section 6. Here, it was demonstrated that the solver functions well for the calculation of the aerodynamic loads on the turbine blade and the integrated rotor plane velocities, provided that input parameters are correctly specified. The reliance of the VPML model on adequately capturing the loading is strongly dependent on accurate specification of the lift and drag coefficients for the aerodynamic sections. These values directly influence the vorticity distribution shed into the wake, which in turn are used by the VPML model. Taking this factor into account however, the qualitative and certainly in some cases quantitative behaviour of the wake is equally captured by the VPML model as compared to an equivalent medium-order method relying on the given aerodynamic definitions.

It is noted that one of the key purposes of implementing the VPML model into QB is the increased efficiency of calculating detailed wake behaviour without the necessity to resort to high power computing resources. The preliminary tests demonstrated in this report represent the first step towards accurate

calculation of wake properties with short calculation times on a modern desktop computer, as all simulations displayed were carried out with total calculation times of the order of 10 minutes. Keeping this in mind, it is noted that further optimization can be achieved and this is considered to be a key future development of the VPML solver.

In future work, further studies will be carried out analysing the influence of stretching and viscous effects on the wake, including an assessment of when their consideration is required. This is expected to be highly dependent upon a number of factors including turbine architecture, environmental conditions and the operating point. As a final note on the application of the solver, it is pointed out that this solution method is also applicable to a range of other turbine architectures including downwind turbines, multi-rotor turbines and vertical axis wind turbines.

9. REFERENCES

1. Van Garrel, A., Multilevel Panel Method for Wind Turbine Rotor Flow Simulations. PhD thesis, University of Twente - Enschede, 2016. Doi: 10.3990/1.9789036542241.

2. Drela, M. XFOIL: An Analysis and Design System for low Reynolds number Airfoils. Proceedings of the Conference on Low Reynolds Number Airfoil Aerodynamics, University of Notre Dame, 1989.

3. Drela , M., Three-Dimensional Integral Boundary Layer Formulation for General Configurations. Proc. 21st AIAA Computational Fluid Dynamics Conference, San-Diego, 2013.

4. Ramos-García, N., Unsteady Viscous-Inviscid Interaction Technique for Wind Turbine Airfoils, PhD Thesis, Technical University of Denmark, 2011.

5. Ramos-García N, Shen WZ, Sørensen JN. Three-dimensional viscous–inviscid coupling method for wind turbine computations. Published online in Wind energy 2014. Doi: 10.1002/we.1821.

6. J. Ferziger J., Milovan, A., Computational Methods for Fluid Dynamics. Aeronautical and Aerospace Engineering, Springer, Berlin, 2002. Doi: 10.1007/978-3-642-56026-20

7. Van Garrel, A., Integral Boundary Layer Methods for Wind Turbine Aerodynamics, Technical Report ECN-C--04-004, 2003. Doi : 10.13140/RG.2.1.3035.9449.

8. Bak,C., Zahle, F., Bitsche, R., Kim, T., Yde, A., Henriksen, L.C., Natarajan, A., Hansen, M., Description of the DTU 10 MW Reference Wind Turbine. DTU Wind Energy Technical Report I-0092, 2013.

9. Burton, T., Jenkins, N., Sharpe, D., Bossanyi, E., Wind Energy Handbook, Wiley, 2011. ISBN 978-0-470-69975-1.

10. Katz, J., Plotkin, A., Low Speed Aerodynamics: From Wing Theory to Panel Methods. McGraw-Hill.

11. Hansen, M.O.L., Aerodynamics of Wind Turbines. Earthscan Publications Ltd., Second Edition, 2008. Doi: 10.4324/9781315769981.

12. Van Garrel, A., Development of a Wind Turbine Aerodynamics Simulation Module. Technical Report ECN-C--03-079. Doi: 10.13140/RG.2.1.2773.8000.

13. Phillips, W.F., Snyder, D.O., Modern Adaptation of Prandtl's Classic Lifting-Line Theory, JOURNAL OF AIRCRAFT, Vol. 37, No. 4. Doi: 10.2514/2.2649.

14. Ang, L., Gaunaa, M., Pirrung, R., Ramos-García, N., Gonzalez Horcas, S., The influence of the bound vortex on the aerodynamics of curved wind turbine blades. The Science of Making Torque from Wind 2020. Doi:10.1088/1742-6596/1618/5/052038.

15. Caprace, D.G., Winckelmans, G., Chatelain, P., An immersed lifting and dragging line model for the vortex particle method. Theoretical and Computational Fluid Dynamics volume 34, pages 21–48 (2020) . Doi: 10.1007/s00162-019-00510-1

16. Sørensen, J.N. and Shen, W.Z., Numerical modelling of wind turbine wakes. Journal of Fluids Engineering. Nr. 2, 2002. Doi :10.1115/1.1471361.

17. Churchfield, M., Schreck, S., Martinez-Tossas, L.A., Meneveau, C., Spalart, P.R., An Advanced Actuator Line Method for Wind Energy Applications and Beyond. Proceedings of the 35th Wind Energy Symposium, Grapevine, Texas, 2017. Doi: 10.2514/6.2017-1998.

18. Martinez-Tossas, L.A., Churchfield, M.J, Meneveau, C., Optimal smoothing length scale for actuator line models of wind turbine blades based on Gaussian body force distribution. Wind Energy, 20, 4, 2017. Doi: 0.1002/we.2081.

19. Sørensen, J.N., Mikkelsen R., Sarmast, S., Ivanell, S., Henningson, D., Determination of Wind Turbine Near-Wake Length Based on Stability Analysis. Journal of Physics: Conference Series. 524 012155, 2014. Doi: 10.1088/1742-6596/524/1/012155.

20. Leweke, T., Le Dizes, S., Williamson, C.H.K., Dynamics and Instabilities of Vortex Pairs. Annual Review of Fluid Dynamics (48), 2016. Doi: 10.1146/annurev-fluid-122414-034558.

21. Vermeer, L.J., Sørensen, J.N., Crespo, A., Wind turbine wake aerodynamics, Progress in Aerospace Science, vol. 39, 2003. Doi :10.1016/S0376-0421(03)00078-2.

22. Widnall, S.E., The stability of a helical vortex filament, Journal of Fluid Mechanics, vol. 54, 1972. Doi :10.1017/S0022112072000928.

23. Jensen, N.O., A Note on Wind Generator Instability, Risø National Laboratory Technical Report M-2411, 1983.

24. S. Frandsen et al., Analytical Modeling of Wind speed Deficit in Large Offshore Wind Farms, Wind Energy 9, 39-53 (2006).

25. Bastankhah, M., Porté-Agel, F., A new analytical model for wind-turbine wakes, Renewable Energy, Vol. 70 , 2014. Doi : 10.1016/j.renene.2014.01.002.

26. Akbar, M., Sørensen, J.N., Porté-Agel, F., An Analytical Model for the Effect of Vertical Wind Veer on Wind Turbine Wakes, Energies 2018, 11(7). Doi : 10.3390/en11071838.

27. Sørensen, J.N., General Momentum Theory for Horizontal Axis Wind Turbines, Springer International Publishing, 2016. Doi: 10.1007/978-3-319-22114-4.

28. Branlard, E., Wind Turbine Aerodynamics and Vorticity Based Methods, Springer International Publishing, 2017. Isbn 978-3-319-85583-7, Doi: 10.1007/978-3-319-55164-7.

29. Winckelmans, G.S., Topics in Vortex methods for the Computation of two- and three-dimensional incompressible unsteady flows. PhD Thesis, CalTech, 1989. Doi : 10.7907/19HD-DF80.

30. Winckelmans, G.S., Leonard, A., Contributions to vortex particle methods for the computation of three-dimensional incompressible unsteady flows, Journal of Computational Physics, Vol. 109, 1993. Doi: 10.1006/jcph.1993.1216.

31. Ploumhans, P. and Winckelmans, G.S., Vortex Methods for High-Resolution Simulations of Viscous Flow Past Bluff Bodies of General Geometry, Journal of Computational Physics, Vol. 165, 2000. Doi: 10.1006/jcph.2000.6614.

32. Cocle, R., Winckelmans, G.S., Daeninck, G., Combining the Vortex-in-cell and Parallel Fast Multipole Methods for Efficient Domain Decomposition Simulations, Journal of Computational Physics, Vol. 227, 2008. Doi: 10.1016/j.jcp.2007.10.010.

33. Papadakis, G., Development of a hybrid compressible vortex particle method and application to external problems including helicopter flows, PhD Thesis, National Technical University of Athens, 2014. Doi: 10.13140/RG.2.2.26480.92168.

34. Marten, D., Lennie, M., Pechlivanoglou, G., Nayeri, C.N., Pachereit, C.O., Implementation, Optimization, and Validation of a Nonlinear Lifting Line-Free Vortex Wake Module Within the Wind Turbine Simulation Code QBlade, J. Eng. Gas Turbines Power. Jul 2016, 138(7). Doi: 10.1115/1.4031872.

35. Barnes, J., Hut, P., A hierarchical O(N log N) force-calculation algorithm, Nature, 1986. Doi: 10.1038/324446a0.

36. Greengard, L., Carrier, J., Rokhlin, V., A Fast Adaptive Multipole Algorithm for Particle Simulations, SIAM J. Sci. and Stat. Comput. (9). Doi:1 0.1137/0909044.

37. Greengard, L., Rokhlin, V., A new version of the fast multipole method for the Laplace equation in three dimensions. Acta Numerica (6), 1997. Doi: 10.1017/S0962492900002725.

38. Van Garrel, A., Venner, C.H., Hoeijmakers, H.W., Fast Multilevel Panel Method for Wind Turbine Rotor Flow Simulations, Proc. AIAA SciTech Forum, Grapevine, Texas, USA, 2017. Doi: 10.2514/6.2017-2001.

39. Schubiger, A., Barber, S., Nordborg, H., Evaluation of the lattice Boltzmann method for wind modelling in complex terrain, Wind Energy Science 5(4):1507-1519, 2020. Doi: 0.5194/wes-5-1507-2020.

40. Pope, S.B., Turbulent Flows, Cambridge University Press, 2000. Isbn 052159125, Doi: 10.1017/CBO9780511840531.

41. Stergiannis, N., Lacor, C., Beeck, J.V., Donnelly, R., CFD modelling approaches against single wind turbine wake measurements using RANS. Journal of Physics: Conference Series, Volume 753, Issue 3. Doi: 10.1088/1742-6596/753/3/032062.

42. Wendler J., Marten, D., Pechlivanoglou, G., Nayeri, C.N., Paschereit, C.O., An Unsteady Aerodynamics Model for Lifting Line Free Vortex Wake Simulations of HAWT and VAWT in QBlade. Proc. ASME Turbo Expo, 2016, 2016. Doi: 10.1115/GT2016-57184.

43. Leishman, J.G., Beddoes, T.S., A Semi-Empirical Model for Dynamic Stall, Journal of the American Helicopter Society, 34 (3), Doi:10.4050/JAHS.34.3.

44. Madsen, H.E., Larsen T.J., Pirrung, G.R., Li, A., Zahle F. Implementation of the blade element momentum model on a polar grid and its aeroelastic load impact, W ind Energ. Sci., 5, 1–27, 2020. Doi:10.5194/wes-5-1-2020.

45. Hejlesen, M.M., A high order regularisation method for solving the Poisson equation and selected applications using vortex methods. PhD Thesis, Danish Technical University, 2016.

46. Saverin, J., Multilevel Vortex Particle Method for Aerodynamic Simulations. PhD Thesis, TU Berlin, 2022. Doi: 10.14279/depositonce-14922

47. Berrut, J.P., Trefethen, L.N., Barycentric Lagrange Interpolation, Siam Review, vol. 26, 2004. Doi: 10.1137/S0036144502417715 .

48. Hejlesen, M.M., Winckelmans, G., Walther, J.H., Non-singular Green's functions for the unbounded Poisson equation in one, two and three dimensions, Applied Mathematics Letters, vol. 89, 2019. Doi: 10.1016/j.aml.2018.09.012.

49. Patra, M., Karttunen, M., Stencils with Isotropic Discretisation Error for Differential Operators, Numerical Methods for Particle Differential Equations, 2006. Doi: 10.1002/num.20129

50. Cottet, G.H. and Koumoutsakos, P.D., Vortex Methods: Theory and Practice, Cambridge University Press, 2007. Doi: 10.1017/CBO9780511526442.

51. Ramos-García, N., Hejlesen, M.M., Sørensen, J.N., Walther, J.H., Hybrid vortex simulations of wind turbines using a three-dimensional viscous-inviscid panel method. Wind Energy (20), 2017. Doi: 10.1002/we.2126.

52. Bortolotti, P., Tarres, H.C., Dykes, K., Merz, S. L., Verelst D. and Zahle F., IEA wind TCP task37: systems engineering in wind energy - WP2.1 reference wind turbines Technical Report.: NREL/TP-5000-73492, US, 2019.

53. Behrens de Luna, R., Marten, D., Barlas, T., Horcas, S.G., Ramos-García, N., Li, A., Paschereit, C.O., Comparison of different fidelity aerodynamic solvers on the IEA 10MW turbine including novel tip extension geometries, Journal of Physics Conference Series. Torque 2022 (Abstract accepted).

54. Sørensen, N.N., Block General Purpose Flow Solver Applied to Flow Over Hills, PhD Thesis, Risø National Laboratory, Roskilde 1995.

55. Boorsma, K., Schepers, J.G., Gomez-Iradi, S., Herraez, I., Lutz, T., Weihing, P., Oggiano, L., Pirrung, G., Madsen, H.A., Shen, W.Z., Rahimi, H., Schaffarczyk, P., Final Report of IEA Wind Task 29 Mexnext (Phase 3), ECN Technical Report ECN-E--18-003.

56. Schepers, J.G. and Snel, H., Model Experiments in Controlled Conditions- Final Report, Technical Report ECN-E-07-042. Doi: 10.1088/1742-6596/753/2/022004.

57. Boorsma, K., Schepers, J.G., New MEXICO experiment. Preliminary overview with initial validation. Technical Report ECN-E--14-048, 2014.

58. Weihing, P., Letzgus, J., Bangga, G., Lutz, T., Krämer, E., Hybrid RANS/LES capabilities of the flow solver FLOWer—Application to flow around wind turbines, Proceedings of the Sixth HRLM Symposium, Strasbourg, France, 2016.

59. Øye, S., Dynamic stall simulated as time lag of separation, Presented at the IEA fourth symposium on the aerodynamics of wind turbines, Rome, 1990. Technical Report ETSU-N-118.

60. Bergami, L., Gaunaa, M., ATEFlap Aerodynamic Model, a Dynamic Stall Model Including the Effects of Trailing Edge Flap Deflection. Smart Rotor Modeling (pp.33-79), 2014. Doi: 10.1007/978-3-319-07365-1_4.

61. Saverin, J., Perez-Becker, S., Behrens de Luna, R., Marten, D., Gilloteaux, J.C., Kurnia, R., Higher order Hydroelastic Module. Technical Report: Deliverable 1.2, FLOATECH Project, European Union: H2020-EU.3.3.2. - Low-cost, low-carbon energy supply EU Project.

62. Howland, M.F., Lele, S.K., Dabiri, J.O., Wind farm power optimization through wake steering, Proceedings of the National Academy of Sciences, 2019. Doi: 10.1073/pnas.1903680116.

63. Leble, V., Barakos, G.N., Forced Pitch Motion of Wind Turbines, Journal of Physics Conference Series. Doi:10.1088/1742-6596/753/2/022042.

64. Platis, A., Sedersleben, S.K., Bange, J., Lampert, A., Bärfuss, K., Hankers, R., Canadilla, B., Foreman, R., Schulz-Stellenfleth, J., Djath, B., Neumann, T., and Emeis, S., First in situ evidence of wakes in far field behind offshore wind farms. Scientific Reports, 8, 2018. doi:10.1038/s41598-018-20389-y